Chem, Volume *8*

Supplemental information

Sol-gel processing of a covalent organic framework for the generation of hierarchically porous monolithic adsorbents

Mark E. Carrington, Nakul Rampal, David G. Madden, Daniel O'Nolan, Nicola Pietro Maria Casati, Giorgio Divitini, Jesús Á. Martín-Illán, Michele Tricarico, Ritums Cepitis, Ceren Çamur, Teresa Curtin, Joaquin Silvestre-Albero, Jin-Chong Tan, Felix Zamora, Sergei Taraskin, Karena W. Chapman, and David Fairen-Jimenez

Supplemental Experimental Procedures

Table of contents:

S1. Slipped TPB-DMTP-COF structures

The crystallographic information file (CIF) of the TPB-DMTP-COF is taken from the CURATED COF database[1]. The TPB-DMTP-COF has weak interlayer coupling and hence is prone to slipping. To find the structure that best represents the monolith synthesized, one of the two layers of the COF is moved from AA stacking to AB stacking. The COF slipping strategy is explained in **Figure S1a**. The turquoise node represents the point at which the two layers are in perfect AA stacking or perfect AB stacking. The turquoise node is then moved to the different yellow points, representing the AA → AB transition structures, which we define as 25%, 40%, 50% and 75% slipped structures. The adsorption isotherms are computed (described in the next section) and the structure for which we get the best fit to the experimental adsorption isotherms is determined to be the 'correct' structure. The different slipped structures are shown in **Figure S1b**.

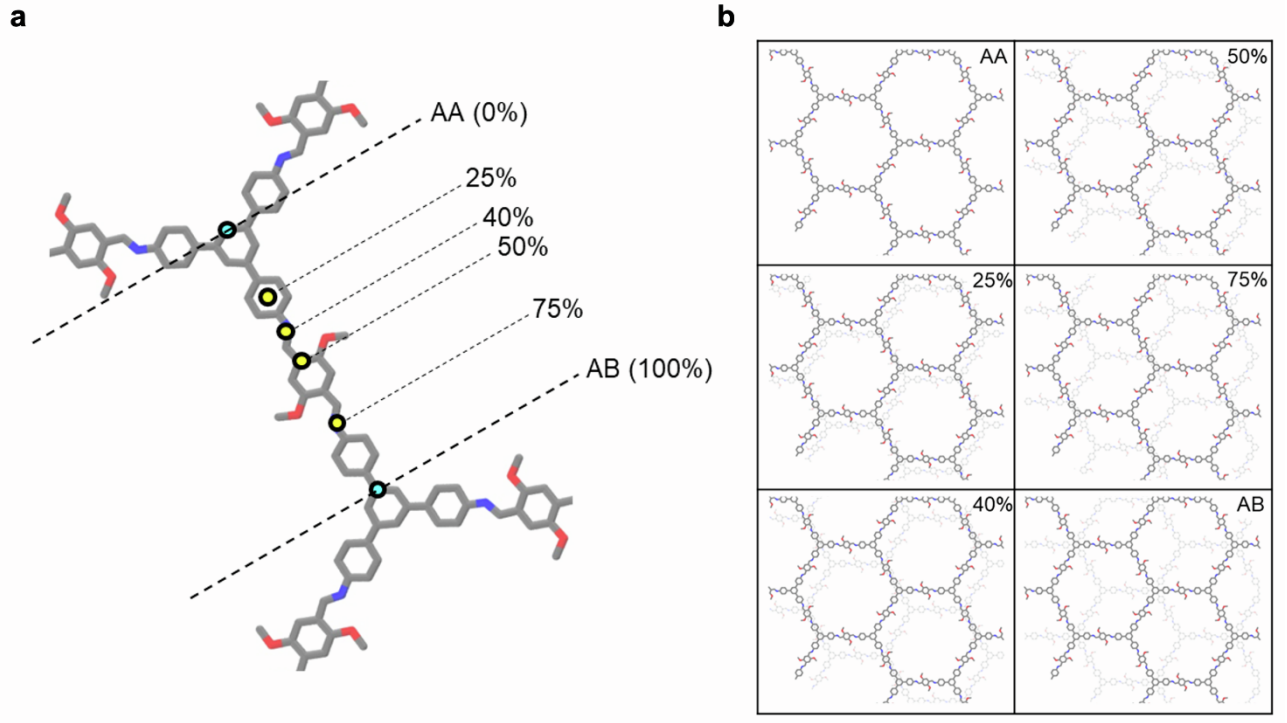

Figure S1 | COF slipping strategy and structures. (a) TPB-DMTP-COF framework is shown with the turquoise nodes representing the perfect AA (0%) and AB (100%) structures; the yellow nodes show the different AA → AB transition states – 25%, 40%, 50%, and 75% slipping. C atoms are in grey; O atoms are in red; N atoms are in blue and H atoms have been omitted for clarity. **(b)** Different COF slipped structures obtained using the strategy described above with layer A in the foreground, and layer B in the background.

S2. Molecular simulation

To make sure that the slipped structures created manually are in their lowest energy state, the geometry of all the structures is optimized using the Forcite module of Accelrys Material Studio. N_2 adsorption isotherms are simulated using the Grand Canonical Monte Carlo method as implemented in the RASPA simulation package. [2] Monte Carlo moves consist of insertion, deletion, rotation, and translation moves, each with equal probabilities. For all the pressure points we use 10,000 cycles for equilibration and another 20,000 cycles to average the properties. A cycle is defined as the maximum of 20 steps or the number of molecules in the system. This implies that, on average, a Monte Carlo move has been attempted on all the molecules during each cycle. Intermolecular interactions are modeled using the Lennard-Jones (LJ) potential with a cutoff of 12.8 Å. Lorentz-Berthelot mixing rules are used for all the cross-interaction terms. Electrostatic interactions are modeled using the coulombic potential and are computed using the Ewald summation method with the precision set to 10^{-6}. N_2 is modelled using parameters taken from the TraPPE force field.[3] **Table S1** shows the parameters used for N_2 in this study. The framework atoms are modeled using LJ parameters taken from the DREIDING force field.[4] **Table S2** shows the LJ parameters used to describe the atoms in the framework. All the frameworks are modeled as rigid structures with periodic boundary conditions applied in all directions. The number of unit cells in the simulation box is computed individually for each of the structures to make sure the simulation box is large enough to ensure that a distance of at least twice the cutoff radius is maintained between the periodic images. The charges for the framework are computed using the EQeq protocol.[5] The geometric properties are calculated using Poreblazer.[6] To better compare the simulated adsorption isotherms with the experimental adsorption isotherms, all the simulated data points have been scaled by a scaling factor. The scaling factor is defined as the ratio of the N_2 loading at $\frac{p}{p_0} \cong 0.6$ seen in the powder to that seen in the GCMC simulations.

Table S1 | Lennard-Jones parameters and charges for N_2. Column 1 lists the name of the adsorbate; column 2 lists the corresponding atom types of the adsorbate, M is the dummy atom of N_2; columns 3, 4 and 5 list their corresponding LJ parameters and charges, σ in Å, ε/K_b in K, and q in e taken from the TraPPE force field.

Adsorbate	Atom	LJ Parameters		q (e)
		σ (Å)	**ε/k_B (K)**	
N_2	N	3.31	36	-0.482
	M	0	0	0.964
	N	3.31	36	-0.482

Table S2 | Lennard Jones parameters for the atoms in the framework. Column 1 lists the atom type; columns 2 and 3 list the Lennard Jones parameters for the corresponding atom types, σ in Å and ε/K_b in K, taken from the DREIDING force field.

Atom	LJ Parameters	
	σ (Å)	**ε/k_B (K)**
C	3.47	47.854
H	2.844	7.65
N	3.26	38.948
O	3.03	48.156

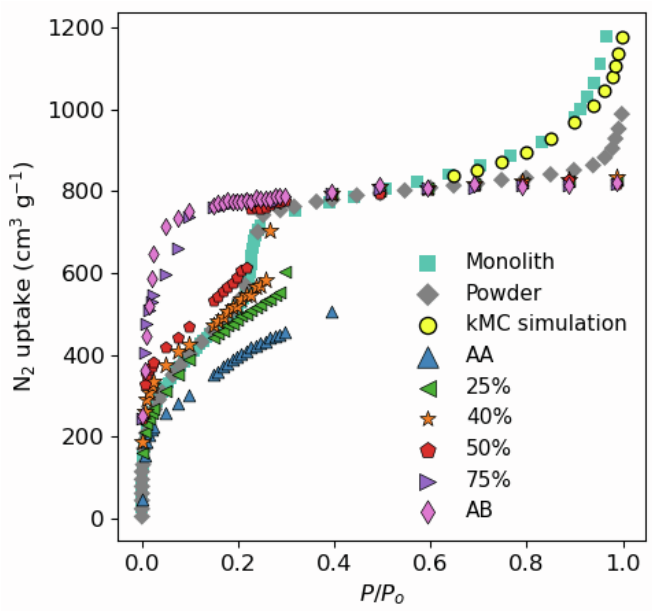

Figure S2 | Comparison of experimental adsorption isotherms to simulated adsorption isotherms of N_2 at 77 K in the different phases of the TPB-DMTP-COF. The experimental adsorption isotherms are represented using the turquoise squares for the monolith (3 bar h^{-1} $scCO_2$ activated 1.000 (v/v)) and grey diamonds for the powder. Simulated adsorption isotherms are represented using the points with a black border; blue (triangle, pointing up) - AA stacked structure; green (triangle, pointing, left) – 25% slipped structure; orange (star) – 40% slipped structure; red (pentagon) – 50% slipped structure; purple (triangle, pointing right) – 75% slipped structure and pink (narrow diamond) – AB stacked structure. All of these points have been obtained using GCMC simulations. The yellow (circle) points are the data points obtained by performing kMC simulations using the lattice gas model.

S3. Experimental characterisation

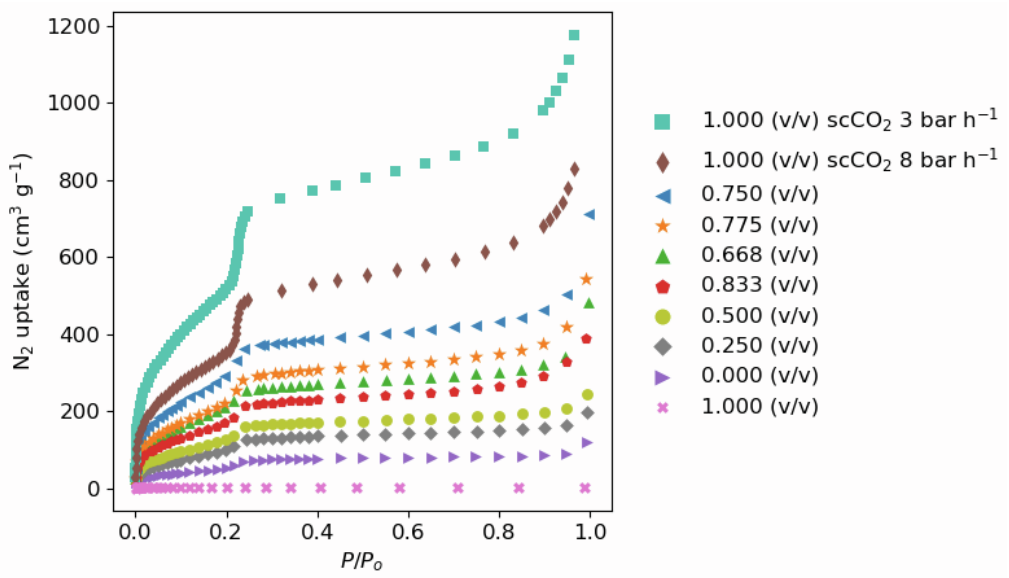

Figure S3 | Comparison of experimental adsorption isotherms of N_2 at 77 K for samples prepared using varying acetonitrile fractions. Turquoise (square) – 3 bar h^{-1} $scCO_2$ activated 1.000 (v/v); brown (diamond, narrow) – 8 bar h^{-1} $scCO_2$ activated 1.000 (v/v); blue (triangle, pointing left) – 0.750 (v/v); orange (star) – 0.775 (v/v); green (triangle, pointing up) – 0.668 (v/v); red (pentagon) – 0.833 (v/v); olive (circle) – 0.500 (v/v); grey (diamond, wide) – 0.250 (v/v); purple (triangle, pointing right) – 0.000 (v/v) and cross (pink) – 1.000 (v/v) collapse.

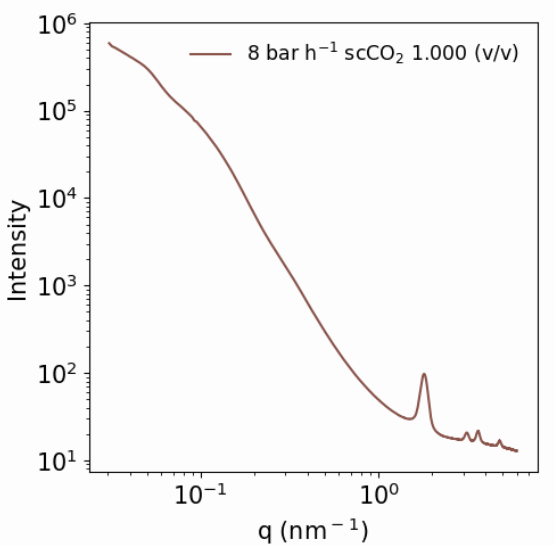

Figure S4 | SAXS data of the supercritically activated (8 bar h^{-1}) 1.000 acetonitrile fraction TPB-DMTP COF monolith (brown).

Table S3 | Textural properties of the TPB-DMTP-COF monolith (3 bar h^{-1} $scCO_2$ activated 1.000 acetonitrile fraction sample) and powder.

Property	Monolith	Powder
Bulk volume (cm^3)	0.2041	0.2686
Bulk density (g cm^{-3})	0.1558	0.2502
Apparent density at FILL (200 μm) (g cm^{-3})	0.1558	0.2502
Apparent density at 1 atm (14μm) (g cm^{-3})	0.1634	0.3211
Sample weight (g)	0.0318	0.0672
Sample porosity (%)	63.8319	89.6476
Total intruded volume (cm^3)	0.1303	0.2408
Mercury surface area (m^2 g^{-1})	504.0448	196.0502

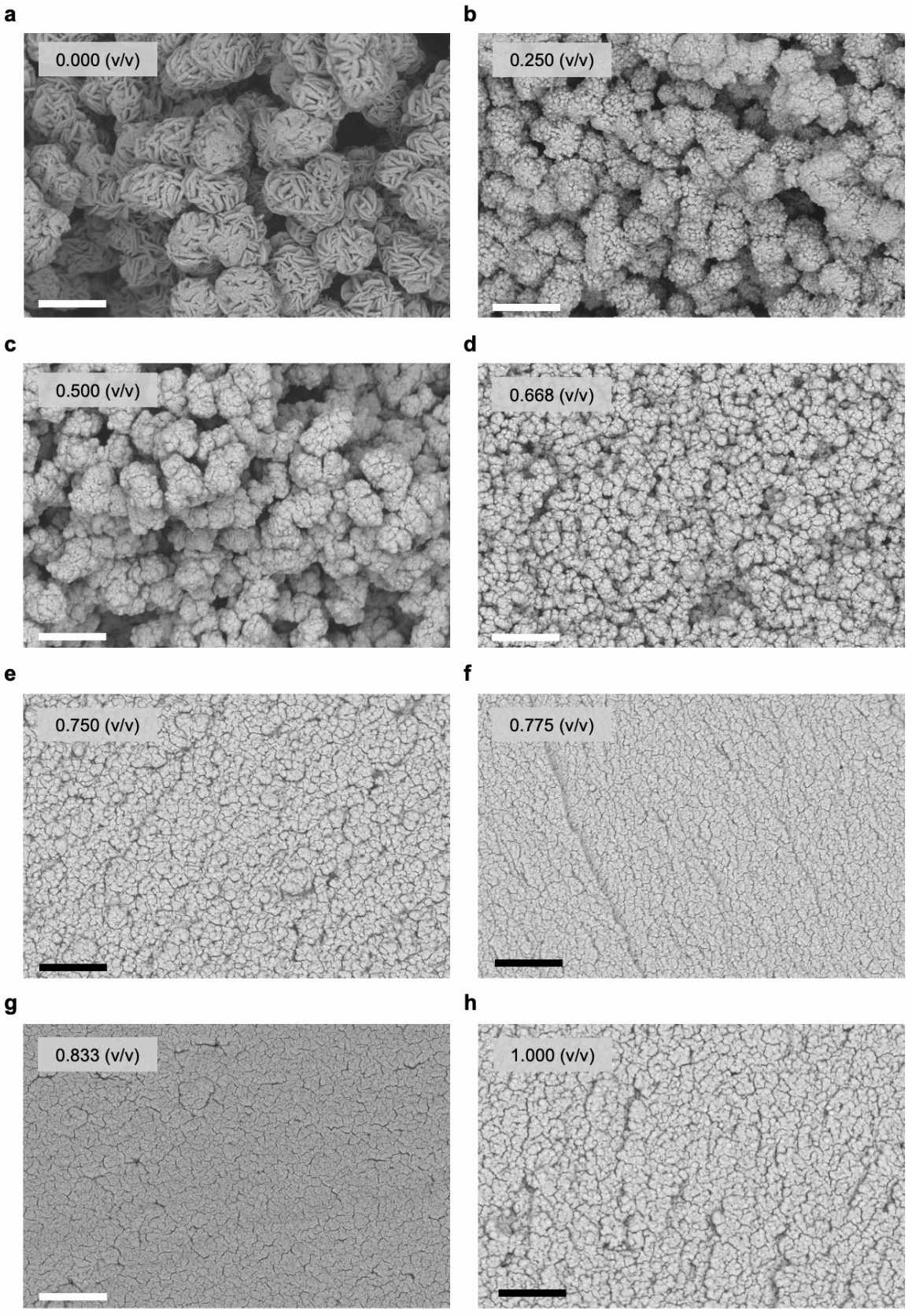

Figure S5 | SEM images of the TPB-DMTP-COF monolith synthesized using varying acetonitrile fractions. **(a)** 0.000 (v/v), **(b)** 0.250 (v/v), **(c)** 0.500 (v/v), **(d)** 0.688 (v/v), **(e)** 0.750 (v/v), **(f)** 0.775 (v/v), **(g)** 0.833 (v/v), and **(h)** 1.000 (v/v). Scale bar is 1 μm.

S4. Lattice gas model

Reconstruction Procedure:

The details of the method for the calculation of the two-point correlation function, $S_2(r)$, from SAXS data described below is based on the works of Kikkinides et al[7] and Debye et al[8, 9]. Within the small-angle isotropic scattering regime, the spherically averaged intensity, $I(q)$, can be represented in the following integral form,

$$I(q) = 4\pi\rho^2 V \int_0^\infty r^2 \gamma(r) \frac{sin\,(qr)}{qr} dr \qquad [1]$$

where, q is the scattering wavevector which is equal to $4\pi(sin\theta)/\lambda$ for isotropic scattering, λ is the wavelength, 2θ is the scattering angle, $\gamma(r)$ is the density fluctuation autocorrelation function, ρ is the electron density of the x-rays and V is the volume of the sample. It is also known that the density autocorrelation function can be related to the two-point correlation function $S_2(r)$ by the expression[10],

$$\gamma(r) = S_2(r) - \varepsilon^2 \qquad [2]$$

where, ε is the porosity of the material. By using an inverse Fourier transform of **equation 1**, we can determine $\gamma(r)$, and then, by using **equation 2** we can calculate $S_2(r)$. The $S_2(r)$ function obtained for the TPB-DMTP-COF monolith according to the procedure described above is shown in **Figure 5b** (see the grey line) in the main text. Thus obtained two-point correlation function $S_2(r)$ can be used for structural reconstruction of the TPB-DMTP-COF monolith. The reconstruction method employed in our work can be framed as an energy-minimization problem by means of simulated annealing and is based on the work of Torquato and co-workers[11-14]. Within this method, we consider a cubic box containing N = 60 x 60 x 60 cells with periodic boundaries (shown as grey (black) cells in **Figure 5a** (**Figure 5c**) in the main text) arranged on a bcc lattice with 1% of the cells occupied by the material (matrix), that is a 'lattice-gas' model structure, with porosity ε = 0.99. The matrix cells are randomly placed on lattice sites within the box at the start of the reconstruction. The reconstruction algorithm consists of a sequence of steps. At every step, for each cell occupied by the material, an empty cell is randomly chosen and occupation of these cells is swapped, so that the empty cells become occupied by material and formerly occupied ones become empty. Such a swap is accepted according to the Metropolis probability[15],

$$P_{accept} = \begin{cases} e^{-\frac{E_f - E_i}{\theta}} & if\ E_f - E_i > 0 \\ 1 & if\ E_f - E_i < 0 \end{cases} \qquad [3]$$

where, E_i and E_f are the initial and final "energies" of the system, respectively, and θ here is the fictive temperature. The "energy" function is defined as the sum of squared differences between the experimentally measured two-point correlation function of the target medium and the two-point correlation function of the reconstructed medium,

$$E = \sum_i \left[S_2^{reconstructed}(r_i) - S_2^{target}(r_i)\right]^2 \qquad [4]$$

where i runs through all occupied cells in the box. The fictive temperature controls the annealing process of reconstruction. The temperature is chosen to be high at the start of the reconstruction thus allowing for exploration of the configuration space. Then the temperature is decreased exponentially, $\theta(k) = 0.95^k\,\theta(0)$, with the number,

k, of the simulation steps. As a result of such an annealing procedure, the structure reaches a minimum in the "energy" space which represents well the experimentally observed structure (see **Figure 5b** in the main text).

Sorption simulations:

The lattice structural model obtained by the reconstruction algorithm can be used for the study of sorption of fluid by porous materials. This can be done within the framework of the well-developed lattice-gas model for fluid sorption in porous media[16-21]. In the lattice gas model, porous media is coarse grained into cells arranged on a regular lattice and each cell can either be occupied by a solid, fluid or vapour. The occupation of each cell is characterized by two occupation variables, η and τ. If a cell i is occupied by the material (matrix) then $\eta_i = 0$ and $\tau_i = 0$. The occupation numbers of all the matrix cells do not change in the course of sorption for a particular reconstructred structural model. The value of η equals unity for all other cells in the lattice and these cells can be in two states: occupied by the fluid, $\tau_i = 1$, or empty (occupied by vapour), $\tau_i = 0$. The structural model is assumed to be in thermal equilibrium with the pool of fluid cells and the statistical behaviour of the system is analysed within the grand canonical ensemble described by the partition function,

$$Z_\mu = \sum_{\{\tau\}} e^{-\beta(\mathcal{H} - \mu \sum_i \eta_i \tau_i)} \quad [5]$$

where the sum in $\{\tau\}$ is taken over all possible configurations τ of the cells occupied by the fluid, μ stands for the chemical potential and β is the inverse temperature in energy units. The lattice-gas Hamiltonian entering the expression for the partition function is given by the following expression,

$$\mathcal{H} = -w_{mf} \sum_{\langle ij \rangle} \left[\tau_i \eta_i (1 - \eta_j) + \tau_j \eta_j (1 - \eta_i)\right] - w_{ff} \sum_{\langle ij \rangle} \tau_i \tau_j \eta_i \eta_j \quad [6]$$

where the summation is performed over all distinct pairs $\langle ij \rangle$ of the nearest neighbour cells i and j . This Hamiltonian depends on the two energy parameters, w_{ff} and w_{mf}, describing the strength of the fluid-fluid and matrix-fluid interactions, respectively. In fact, the energy scale can be defined by e.g. the value of w_{ff} and the model effectively depends only on a single parameter, $y = w_{mf}/w_{ff}$, called wettability. The value of y depends on the nature of the fluid and the type of solid studied.

The sorption trajectories of the system in the grand canonical ensemble can be found by means of kinetic Monte Carlo (kMC) simulations, also known as the N-fold Monte-Carlo method, details of which can be found in Refs [22, 23]. In order to model the adsorption of N_2 at 77 K (i.e. $\beta = 0.013$ in inverse energy units), the value of wettability is set to $y = 2.5$[24]. Technically, the adsorption isotherms were obtained by calculating the relative mean fluid density, $\rho_f = N^{-1}\langle \sum_i^N (\eta_i \tau_i) \rangle$, for fixed values of chemical potential, which were varied in small increments of $\Delta\mu = 5$ from -300 to the final value 195. At each value of μ, averaging over 10^3 fluid configurations within the grand-canonical ensemble was performed. The resulting isotherm (see the circles in **Figure 5(d)** of the main text) is continuous indicating that the system is in the supercritical regime for the studied set of parameters.

In order to compare the adsorption isotherms obtained experimentally and numerically (cf. squares and circles in **Figure 5(d)** of the main text), the values of the chemical potential μ were converted to the relative pressure, $\frac{p}{p_0}$, and the values of the mean fluid density to absolute loadings measured in units of $cm^3\ g^{-1}$. To better compare the simulated adsorption isotherms with the experimental adsorption isotherms, all the simulated data points have been scaled by a scaling factor. The scaling factor is defined as the ratio of N_2 loading at $\frac{p}{p_0} \cong 1$ observed experimentally in the monolith to that found in the kMC simulations.

S5. Mechanical properties calculation

In the 'constant strain approach', the process starts by removing the symmetry from the system, followed by an optimization of the cell parameters of the structure. Next, for each configuration, a number of strains are applied resulting in a strained structure. The resulting structure is then optimized again while keeping the cell parameters fixed. The stress and strain tensors obtained are then used to calculate the mechanical properties. The equations used to calculate the different mechanical properties are as follows:

Young's Modulus (E) in each Cartesian direction:

$$E_x = \frac{1}{S_{11}}, \qquad E_y = \frac{1}{S_{22}}, \qquad E_x = \frac{1}{S_{33}} \qquad [7]$$

where s is the elastic compliance and the subscripts indicate the different components.

Voight, Reuss and Hill bulk modulus (K):

$$K_{Voigt} = \frac{1}{9}\left(c_{11} + c_{22} + c_{33} + 2(c_{12} + c_{13} + c_{23})\right) \qquad [8]$$

$$K_{Reuss} = \frac{1}{(s_{11}+s_{22}+s_{33}+2(s_{12}+s_{13}+s_{23}))} \qquad [9]$$

$$K_{Hill} = \frac{K_{Voigt}+K_{Reuss}}{2} \qquad [10]$$

where s is as defined above, c is the independent elastic constant and the subscripts indicate the different components.

Voigt, Reuss, and Hill shear modulus (G):

$$G_{Voigt} = \frac{1}{15}(c_{11} + c_{22} + c_{33} + 2(c_{44} + c_{55} + c_{66}) - c_{12} - c_{13} - c_{23}) \qquad [11]$$

$$G_{Reuss} = \frac{15}{4(s_{11}+s_{22}+s_{33}-s_{12}-s_{13}-s_{23})+3(s_{44}+s_{55}+s_{66})} \qquad [12]$$

$$G_{Hill} = \frac{G_{Voigt}+G_{Reuss}}{2} \qquad [13]$$

where s and c are as defined above and the subscripts indicate the different components. For isotopic materials, the Voigt and Reuss elastic moduli represent the upper and lower limits and hence an average, represented using the Hill elastic moduli, is a good representation of the mechanical properties of the material[25]. Therefore, in this study we report the Hill elastic moduli of the different COFs in the database. The calculation quality is set to ultra-fine and the DREIDING force field parameters are used to model the atoms of the framework.

The COFs are classified as hexagonal based on their space group numbers; any structure with a space group number in the range of 168-194 is classified as a hexagonal crystal.

S6. Total scattering data

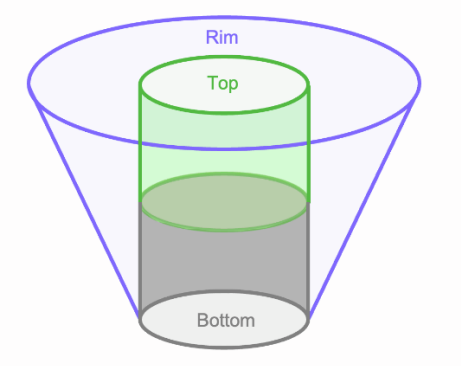

Figure S6 | Monoliths are segmented into different sections to probe structural variation through space. Rim of the monolith (purple), top of the monolith (green), and bottom of the monolith (grey).

Raw data analysis

There are variations on the integrated scattering intensity that reflects the density of the packed sample within the sample capillary. A higher integrated intensity either reflects a higher density within individual sample grains, or a denser packing of the sample grains themselves. We expect that the latter is true, with a denser packing reflecting a smaller grain size. In this way, the density is expected to be related to the mechanical stability of the monolith. The density is anomalously high for the 0.888 (v/v) and 0.944 (v/v) samples. The 1.000 (v/v) monolith (obtained *via* the acetonitrile-scCO$_2$ method) exhibits an exceptionally lower density similar to those along the monotonic trend obtained *via* the acetonitrile-methanol method (**Figure S8**). There was less variability in the density for the rim segments.

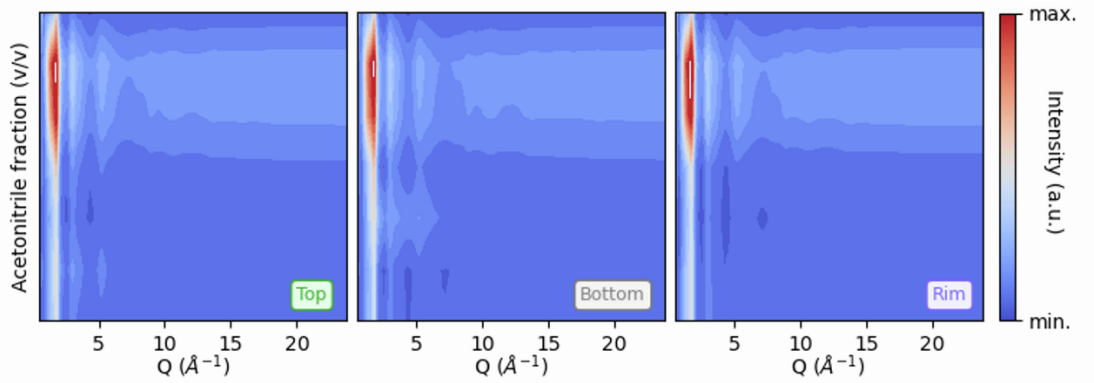

Figure S7 | X-ray diffraction contour plots of monolith samples. Bottom of contour plot exhibits lowest acetonitrile fraction; top exhibits highest acetonitrile fraction.

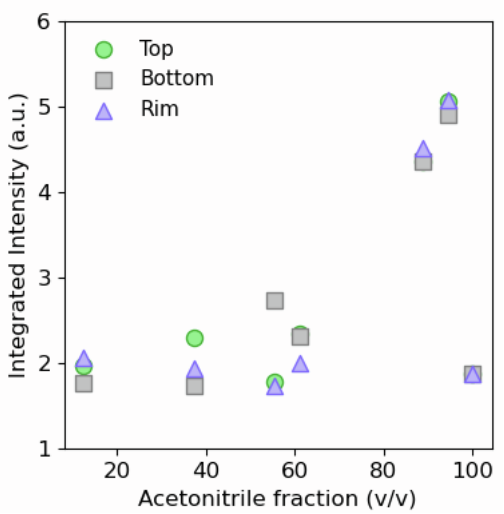

Figure S8 | Trend of density (integrated intensity) as a function of acetonitrile fraction. Integrated intensity determined using the top of the monolith (green circles), bottom of the monolith (grey squares), and top of the monolith (purple triangles). 3 bar h^{-1} $scCO_2$ activated 1.000 (v/v) sample exhibits density consistent with those for low acetonitrile fraction monoliths.

The differences in the diffraction data are more clearly identified in the structure-function data, S(Q) (**Figure S9**). The first peak can be observed to be significantly broader for 0.888 (v/v) and 0.944 (v/v) monolith samples compared to the other samples.

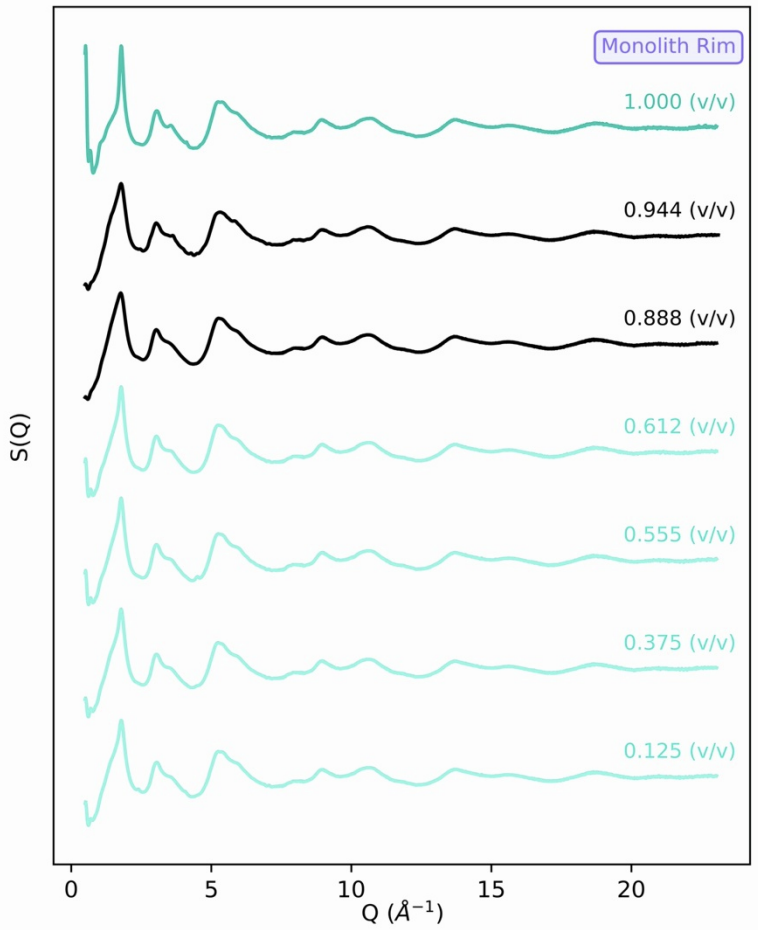

Figure S9 | Total structure function (*S(Q)*) for samples segmented from the rim of monolithic samples.

The pair distribution function (PDF) data (**Figure S10**) exhibit similar peaks in the low-r region, with the first three peaks (*ca.* 1.4, 2.4, and 2.8 Å) being attributable to the 1,2-distances within the covalently bonded structure. These similarities at low *r* are expected as all samples share the same covalent bond connectivity. At higher *r*, larger differences are observed. Long range peaks are observable for low acetonitrile fraction samples synthesized *via* the acetonitrile-methanol method and the 3 bar h^{-1} $scCO_2$ activated 1.000 (v/v) monolith sample obtained *via* the acetonitrile-$scCO_2$ method. At higher acetonitrile fractions (0.888 and 0.944 (v/v)), the high *r* range peaks are significantly reduced.

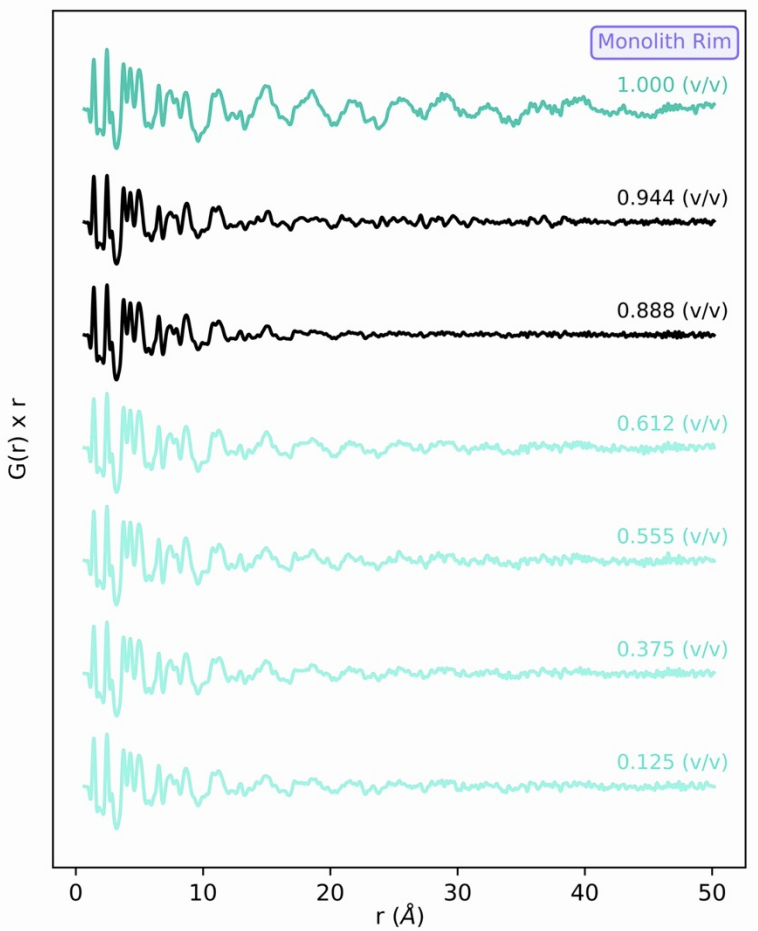

Figure S10 | Pair Distribution Function data for samples segmented from the rim of monolithic samples. *G(r)* is scaled as a function of *r* to emphasize long-range features in the PDF.

Non-negative matrix factorisation

Multivariate analysis of the data was applied to separate the data into fewer components with variable weighting.[26] Here, we applied non-negative matrix factorisation (NMF).[27] NMF is an algorithmic approach wherein an input dataset field (X) is factorized into two matrices which describe the features (W) and their coefficients (H) (**Figure S11**). The algorithm aims to minimize the square error (F^2) of the calculated matrices such that:

$$\|X - WH\|_{F^2} \qquad [14]$$

An advantage of NMF is that it affords inherently positive contributions and therefore derives components more readily interpretable as 'real'.[28] To maintain positive contributions in this step, PDFs were normalized between 0 and 1.

Both diffraction and PDF data for each sample were used to derive NMF components. The PDF data was first boxcar averaged (window = $(2\pi)/Q_{max}$) to reduce the influence of Fourier ripples in the analysis. The NMF analysis was implemented in Python (scipy.decomposition.NMF)[29] with at least 99.9% of the variance within the data explained by three components **(Figure S12)**.

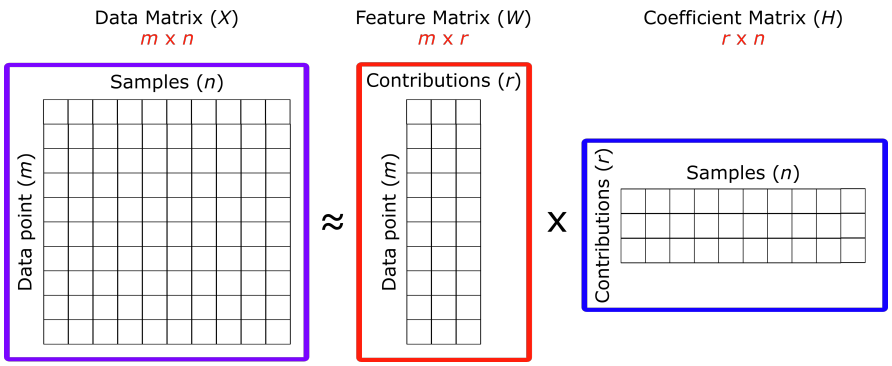

Figure S11 | Non-negative matrix factorisation (NMF) decomposes a data matrix (X) into its underlying components (W) and the weighting of each component (H) for each sample in X.

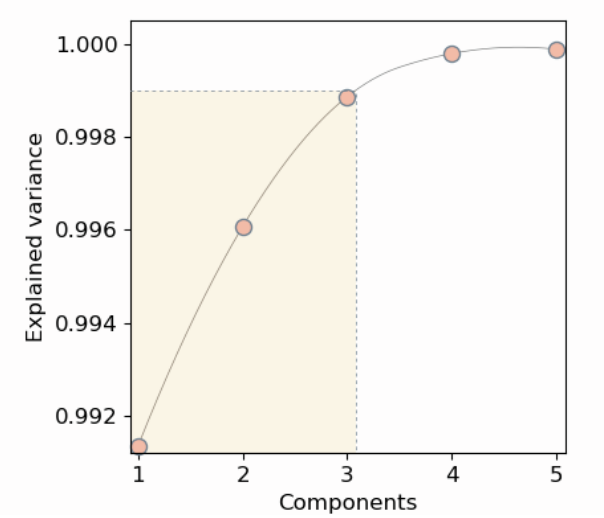

Figure S12 | Variance explained by number of components as observed from the NMF algorithm. 99.9% of variance in the data was explained by three underlying components.

NMF Component Analysis

Indeed, the largest diffraction peak in component **A** (*d*-spacing ≈ 3.742 Å; *Q* ≈ 1.679 Å^{-1}) compares well with the calculated pattern for the AA polymorph peak corresponding to the (001) plane (**Figure S13**). As also observable in their PDFs, component **C** exhibits a similar diffraction pattern to component **A**, yet more diffuse owing to the lower probability of long-range atom-atom correlations (*vide infra*). In contrast, component **B** exhibits broad diffuse scattering consistent with disordered systems.

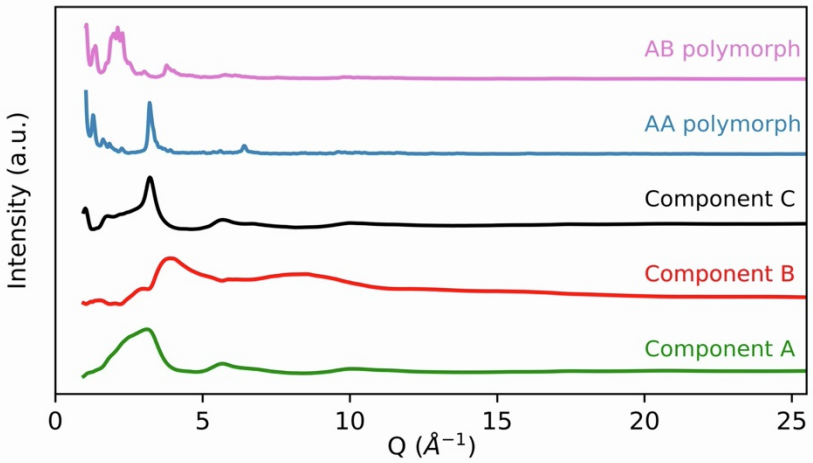

Figure S13 | NMF-derived X-ray diffraction components compared to the calculated diffraction patterns of the AA and AB polymorphs of TPB-DMTP COF. Calculated diffraction pattern for the AB polymorph is in pink, and for the AA polymorph in blue; NMF-derived X-ray diffraction components: Component A is in green, Component B in red, and Component C in black.

The PDFs of components **A** and **C** exhibit similar trends in the low *r* region to those observed in the raw data: atom-atom correlations consistent with those of the covalent bonds in TPB-DMTP-COF (**Figure S14**). However, at higher r, component **A** exhibits limited peak amplitude suggesting limited-to-no correlations between stacking layers (perhaps representative of a single layer). Component **C** has prominent peaks to approximately 36 Å; we observe peaks that have an average repeat distance of *ca.* 3.517 Å (**Figure S15**), consistent with an interlayer separation. The lowest *r* peak in component **B** occurs at a longer distance than in components **A** or **C** (1.56 Å, c.f. 1.40 Å), which suggests that this component includes a significant fraction of longer sp^3-sp^3 carbon-carbon bonds, indeed the second peak in component **B** (2.57 Å) corresponds well to sp^3 hybrid orbital bond angles (110.9°, c.f. 109.5°) which may correspond to unreacted reagent molecules.

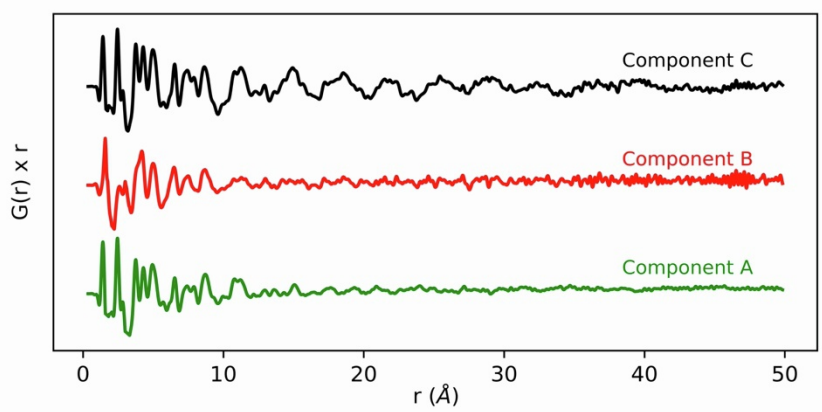

Figure S14 | NMF-derived pair distribution function components. By comparison, component A and C exhibit the same local structure, but C has atom-atom correlations to much further distances. *G(r)* is scaled as a function of *r* to emphasize long-range features in the PDF.

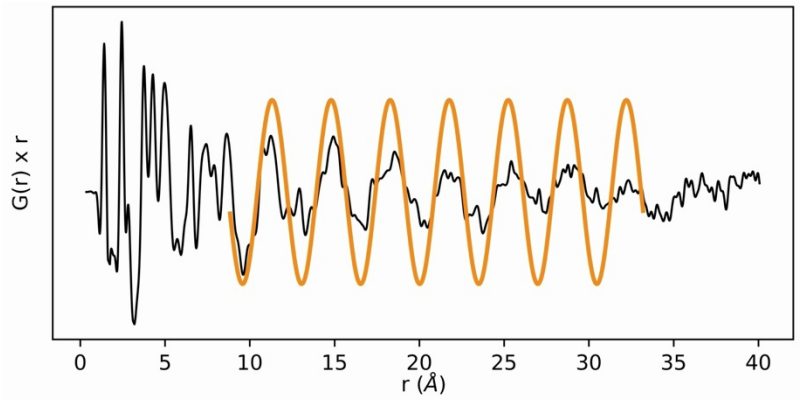

Figure S15 | Pair distribution function of Component C; the overlay sine wave (orange line) exhibits a frequency of 3.517 Å consistent with the stacking distance of consecutive layers. *G(r)* scales as a function of *r* to emphasize the stacking sequence.

Given the discrepancy between diffraction *d*-spacing of the (001) reflection and the stacking distances inferred from PDF data, turbostratic disorder is expected. Changes in stacking sequence can be infinitely uncountable (indeed, in this instance, analysis of stacking faults gave no discernible insight into the structure of monoliths), the hexagonal symmetry of the COF layers allows rotation between layers (θ_i) to be infinitely countable for $-\pi/6 < \theta < \pi/6$. It has previously been shown that structures will exhibit Moiré patterns at angles which satisfy:[30,31]

$$cos(\theta_i) = \frac{3i^2+3i+1/2}{3i^2+3i+1}, \quad i = 0, 1, 2, n \qquad [14]$$

where $i = 0$ affords no turbostratic rotation. We chose to calculate the PDF for TPB-DMTP-COF layers exhibiting AA, AB, and ABC stacking sequences with θ_0, θ_1, *and* θ_2 turbostratic rotation, using a Q_{damp} of *ca.* 0.04 obtained from refinement of a CeO_2 standard and U_{11}, U_{22}, and U_{33} set to 0.005 $Å^2$ with cross diagonal terms set to zero and Q_{max} = 23.12 $Å^{-1}$. Consistent with the shift in the diffraction data, the PDF AA polymorph with the most turbostratic disorder (θ_2) calculated afforded the best comparison to components **A** and **C**.

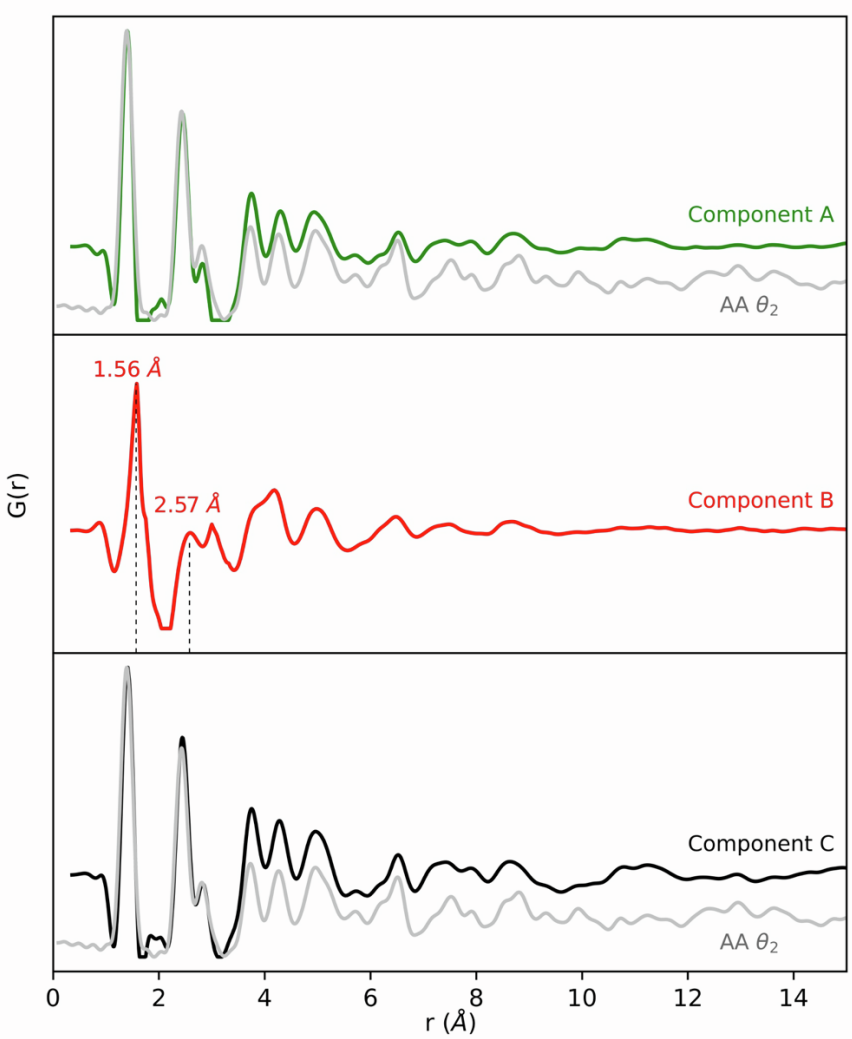

Figure S16 | Fittings to components A, B and C. Components A (green line) and C (black line) are fitted well with a calculated PDF for a TPB-DMTP COF structure with an AA stacking and Moiré turbostratic rotation (grey line). The first two peaks (1.56 Å and 2.57 Å) of component B are consistent with sp^3-sp^3 C-C bonds.

Conclusions

Total scattering analysis of monolithic TPB-DMTP COF structures shows that density increases rapidly at higher acetonitrile fractions for methanol-activated samples (specifically 0.888 and 0.944 (v/v)), which we attribute to mechanical disruption of the structure observable with porosimetry. In contrast, the 3 bar h^{-1} $scCO_2$ activation afforded the 1.000 (v/v) monolith structure with a density like those found for lower acetonitrile fraction methanol-activated samples. Corroborating with surface area measurements suggests that this process avoids the mechanical disruption prone to high acetonitrile fraction samples. To further probe the underlying structural nature of these monoliths, the raw data could be decomposed into 3 underlying components whose fractional weightings vary between monoliths. The data suggests there is a minor content of unreacted compounds, with most of each monolith being a ratio of two structures which exhibit a predominantly AA stacking and whose layers exhibit poor correlations attributable to turbostratic behaviour. The only distinct difference is the range of well-defined atom-atom correlations. As the acetonitrile fraction increases for the methanol activated samples, the presence of the short-range ordered structure decreases until the 0.888 and 0.944 (v/v) monolith samples which again show a sharp increase in this short-range order structure. The 3 bar h^{-1} $scCO_2$ activated 1.000 (v/v) monolith sample exhibits the highest content of the long-range ordered structure.

In connection with the surface area analysis, the propagation of long-range ordered COF affords monoliths with the highest surface area. Using $scCO_2$ is crucial in the synthesis procedure as it circumnavigates the mechanical disruption afforded by methanol activation at high acetonitrile fractions.

S7. PXRD and SAXS analysis

PXRD

Powder X-ray diffraction (PXRD) patters were recorded with a Bruker D8 diffractometer using Cu $K_{\alpha 1}$ (λ = 1.5405 Å) radiation in Bragg Brentano parafocusing geometry with a step of 0.03° at a scan speed of 1.5 s per step.

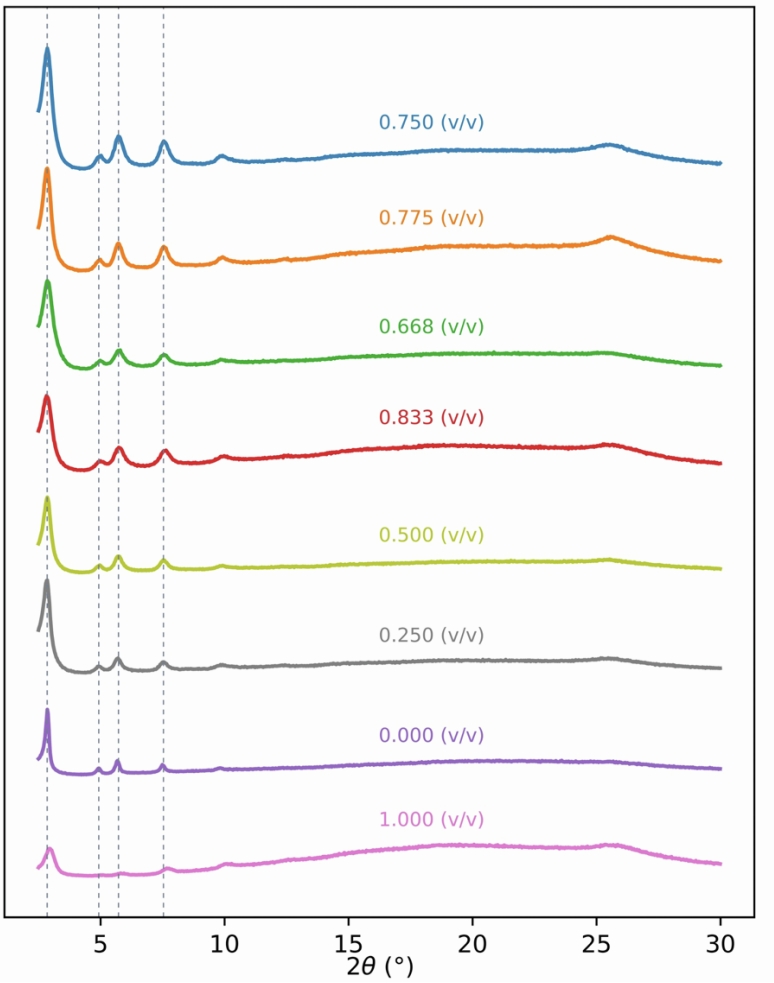

Figure S17 | **PXRD patterns for methanol activated TPB-DMTP-COF monoliths synthesised using varying acetonitrile fractions (v/v).** Methanol activated 1.000 (v/v) is in pink; 0.833 (v/v) is in red; 0.775 (v/v) is in orange; 0.750 (v/v) is in blue; 0.668 (v/v) is in green; 0.500 (v/v) is in olive; 0.250 (v/v) is in grey, and 0.000 (v/v) is in purple. The samples have been arranged in decreasing order of BET areas (from top to bottom).

SAXS

Data were collected at the Materials Science beamline at the Paul Scherrer Institute[32], CH, using a wavelength of 1.0000 Å, as calibrated by the diffraction of a Si NIST standard on the high-resolution powder diffractometer. The beam was restricted *via* primary slits before the monochromator and by two sets of slits before the sample to 0.1 x 0.1 mm. All samples were pre-heated overnight at 120 °C in an evacuated oven and measured within 10 minutes of being extracted. Monolithic samples were held in air while powder samples were loaded in a quartz glass capillary. Acquisition of air and of an empty capillary from the same batch were made immediately after the sample acquisition, in all cases transmission was measured using the filtered primary beam directly on the Mythen II detector with and without sample. A beam-stop was placed midway between the sample and a Pilatus 6M detector. Its position with respect to the samples was calibrated using an Ag behenate sample and using the Dioptas software; the scattering range was 0.0044 $Å^{-1} \leq Q \leq 0.6576$ $Å^{-1}$. Air scattering collected immediately after sample data collection was used as background and was subtracted from the sample data. Data was analyzed in the scattering range 0.0054 $Å^{-1} \leq Q \leq 0.6576$ $Å^{-1}$ using the IRENA package in Igor.[33]

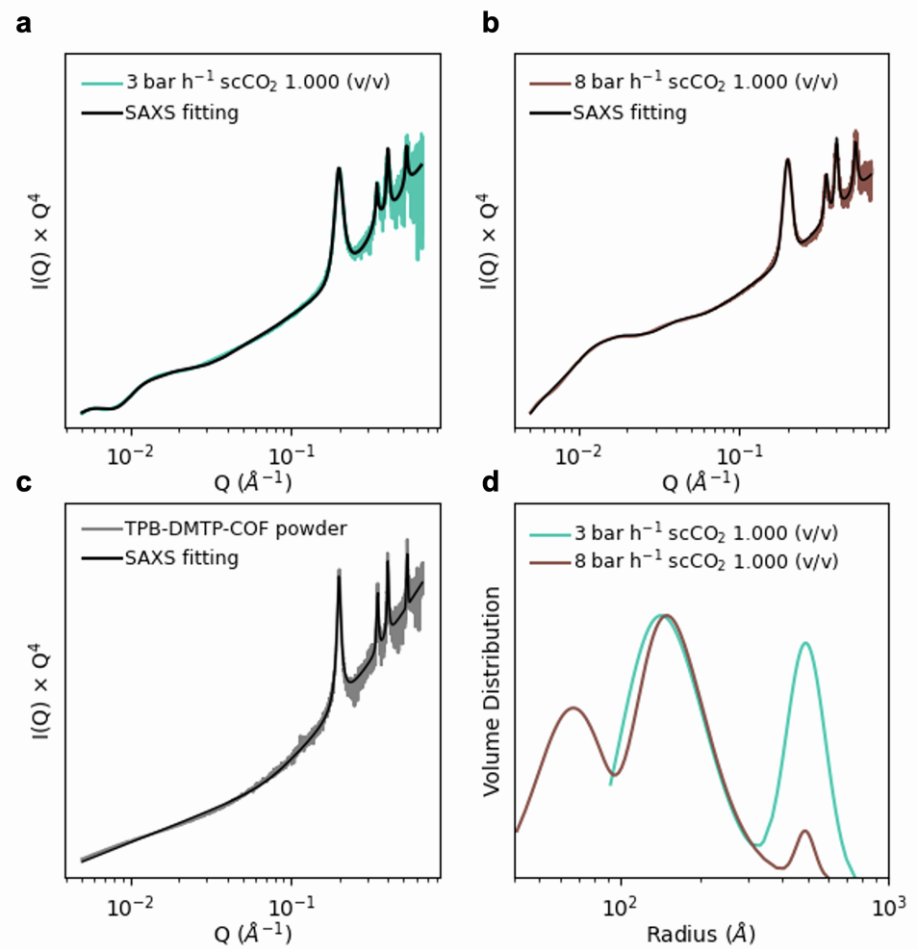

Figure S18 | SAXS fittings and particle size distributions. (a-c) SAXS fittings to TPB-DMTP COF monoliths and powder **(d)** relative volume distribution curve calculable for monolithic and powder structures. Experimental data for the monoliths: 3 bar h^{-1} $scCO_2$ 1.000 (v/v) is in turquoise and 8 bar h^{-1} $scCO_2$ 1.000 (v/v) is in brown, for the TPB-DMTP-COF powder is in grey and the calculated data is in black.

Table S4 | Refined values from SAXS analysis of TPB-DMTP COF samples.

Sample	Size Dist. 1* (Å)	Size Dist. 2* (Å)	Size Dist. 3* (Å)	P**
3 bar h^{-1} $scCO_2$ 1.000 (v/v)	998.0 (σ = 0.2)	257.7 (σ = 0.4)	N/A	-2.8
8 bar h^{-1} $scCO_2$ 1.000 (v/v)	985.1 (σ = 0.1)	210.5 (σ = 0.6)	146.9 (σ = 0.3)	-2.4
TPB-DMTP-COF Powder	N/A	N/A	N/A	-3.1

*Average Particle Diameter; **P = power law slope

Data for the 3 bar h^{-1} $scCO_2$ activated 1.000 acetonitrile fraction monolith (2125 m^2 g^{-1}) were well fit by a model with spheroidal particles with two log normalized-distributions models with mean diameters of 998.0 Å (σ = 0.2) and 257.7 Å (σ = 0.4). The 8 bar h^{-1} $scCO_2$ activated 1.000 acetonitrile fraction sample (1439 m^2 g^{-1}) was fit with three spheroidal size-distribution models exhibiting mean diameters of 985.1 Å (σ = 0.1), 210.5 Å (σ = 0.6), and 146.9 Å (σ = 0.3). This third size population observed for the 8 bar h^{-1} $scCO_2$ activated 1.000 (v/v) monolith are particularly small in size but represents a significant volume fraction. Comparing the relative volume fractions of particle populations, both monoliths have similar concentrations of the *ca.* 230 Å diameter particles, while the 3 bar h^{-1} $scCO_2$ activated 1.000 (v/v) monolith has significantly higher concentrations of the *ca.* 1000 Å diameter particles. The relative populations coincide with the observed density (integrated intensity) of the total scattering data as well as surface area measurements. A size distribution for the powder sample was linked to scattering features beyond the Q-range analyzed here and was not fit.

A power law slope was applied to better model the Porod region of the data. The power law can be related to the form factor of features within the sample. Expectedly for monolithic structures, we did not observe a smooth, simple form factor for these structures. The power law slope for both monoliths was *ca.* -2.8 (3 bar h^{-1} $scCO_2$ activated 1.000 (v/v) monolith - 2125 m^2 g^{-1}) and *ca.* -2.4 (8 bar h^{-1} $scCO_2$ activated 1.000 (v/v) monolith - 1439 m^2 g^{-1}), which is observed for mass fractal structures associated with non-equilibrium growth processes such as percolation clusters or diffusion limited aggregates,[34] consistent with the low-density/high surface areas observed in these materials. In contrast, the porous powder sample exhibited a power law slope of *ca.* -3.1, which is observed for rough fractal surfaces.

S8. IAST selectivity

The selectivity for the adsorbate mixture composition of interest were predicted from the single-component adsorption isotherms using Ideal Adsorbed Solution Theory (IAST).[35] First, the single-component isotherms for the adsorbates at 298 K were fitted to the dual-site Langmuir-Freundlich equation:

$$q = \frac{q_{sat,1}(b_1P)^{\gamma_1}}{1+(b_1P)^{\gamma_1}} + \frac{q_{sat,2}(b_2P)^{\gamma_2}}{1+(b_2P)^{\gamma_2}} \qquad [16]$$

In this equation, q is the amount adsorbed per mass of material (in mol kg^{-1}), P is the total pressure (in bar) of the bulk gas at equilibrium with the adsorbed phase, $q_{sat,1}$ and $q_{sat,2}$ are the saturation uptakes (in mol kg^{-1}) for sites 1 and 2, b_1 and b_2 are the affinity coefficients (in bar^{-1}) for sites 1 and 2, and γ_1 and γ_2 represent the deviations from the ideal homogeneous surface (unit-less) for sites 1 and 2. The parameters that were obtained from the fitting for all the three compounds are found in **Table S5**, respectively. The final selectivity for adsorbate *i* relative to adsorbate *j* was calculated using the following:

$$S_{i/j} = \frac{x_i}{x_j}\frac{y_j}{y_i} \qquad [17]$$

Here, x_i and x_j are the mole fractions of components *i* and *j*, respectively, in the adsorbed phase, and y_i and y_j are the mole fractions of components *i* and *j*, respectively, in the gas phase.

Table S5 | Dual-site Langmuir-Freundlich isotherm fitting parameters for adsorption isotherms of CO_2, N_2, and CH_4 at 298 K for the TPB-DMTP-COF monolith and powder.

Gas	γ_1	γ_2	b_1 (bar^{-1})	b_2 (bar^{-1})	$q_{sat,1}$ (mol kg^{-1})	$q_{sat,2}$ (mol kg^{-1})
Monolith						
CO_2	1.0751	1.25882	11.22648	0.139758	3.79795	204.617
N_2	1.65639.	0.352727	0.260059	4.620e-8	22.4966	41.3899
CH_4	1.43659	0.773592	0.175863	0.033063	75.363	18.6587
Powder						
CO_2	1.13356	2.62E-05	0.22426	1142.524	98.5843	1.14E-16
N_2	1.29787	99.9901	0.35065	1204.367	17.2196	5.11E-09
CH_4	1.51317	2.77973	0.52871	9.539918	24.9342	0.400293

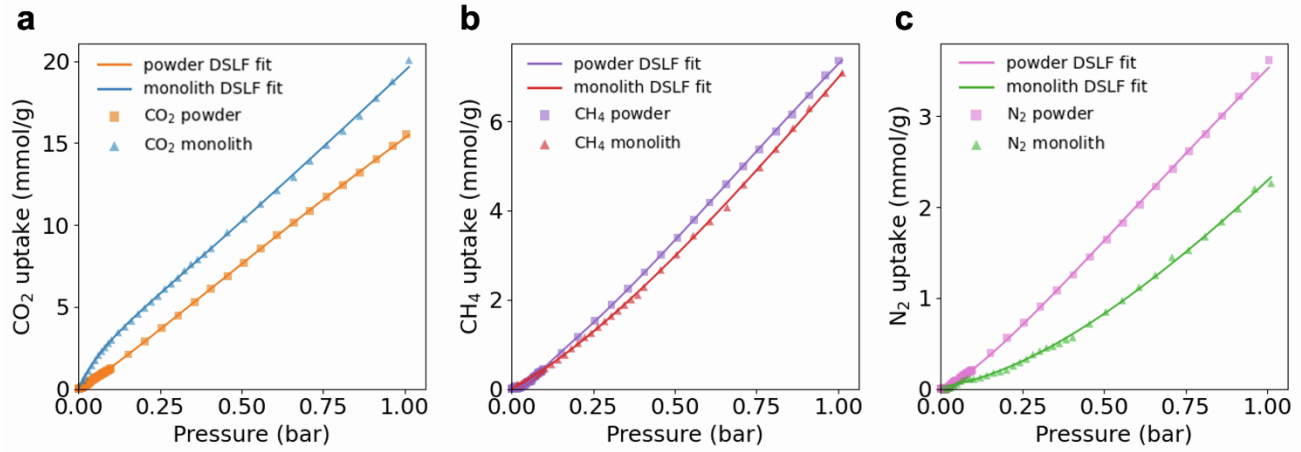

Figure S19 | Dual-site Langmuir-Freundlich (DSLF) isotherm fittings vs experimentally measured isotherms at 298 K. **(a)** CO_2 adsorption isotherms for the powder (orange squares) and monolith (blue triangles) with DSLF fittings in orange (powder) and blue (monolith) **(b)** CH_4 adsorption isotherms for the powder (purple squares) and monolith (red triangles) with DSLF fittings in purple (powder) and red (monolith) **(c)** N_2 adsorption isotherms for the powder (pink squares) and monolith (green triangles) with DSLF fittings in pink (powder) and green (monolith)

S9. BET area calculation using BETSI

BETSI[36] is based on the original Rouquerol criteria for reporting BET areas, but is modified to prevent manual interaction. The only input data required is the adsorption isotherm.

The Rouquerol criteria is as follows:

Regression criteria:

- The linear range should span at least 10 points.
- The R^2 should be greater than or equal to 0.995.

Validity criteria:

1. Over the entire fitting range, $N(1-\frac{P}{P_0})$ must increase monotonically with $\frac{P}{p_0}$.
2. The value of C obtained by linear regression must be positive.

Self-consistency criteria:

1. The monolayer loading, when reported on the isotherm, $N_m(Read)$, must correspond to a pressure that lies in the linear region.
2. The relative pressure corresponding to the monolayer loading as obtained from BET theory, $\frac{p}{p_0}\ (N_m\ BET)$ must be equal to the pressure determined in criterion 3 within a 20% tolerance.

A detailed explanation of the output obtained from BETSI is given in **Figures S20** and **S21**.

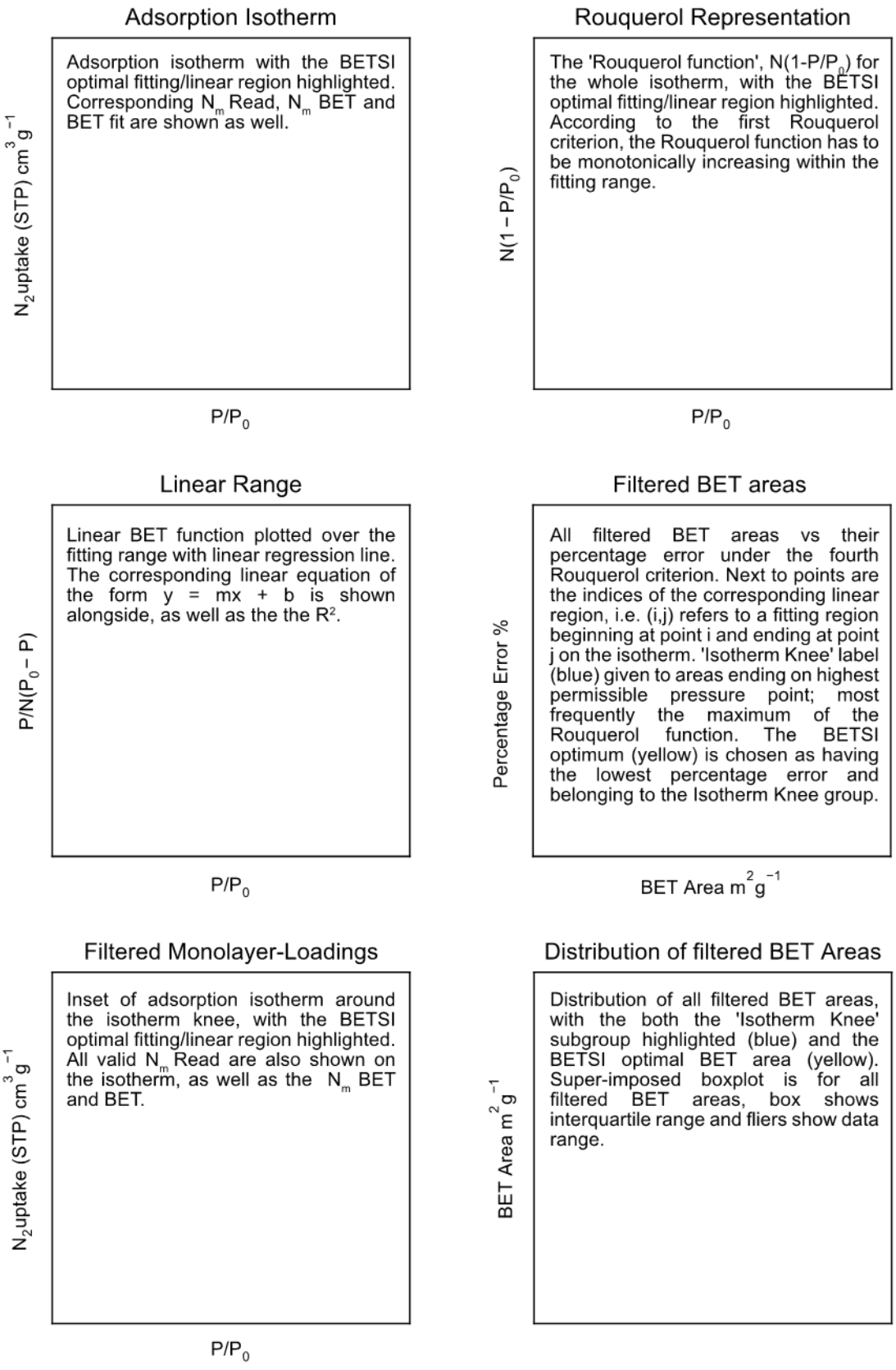

Figure S20 | Description of the different plots obtained in a BETSI analysis.

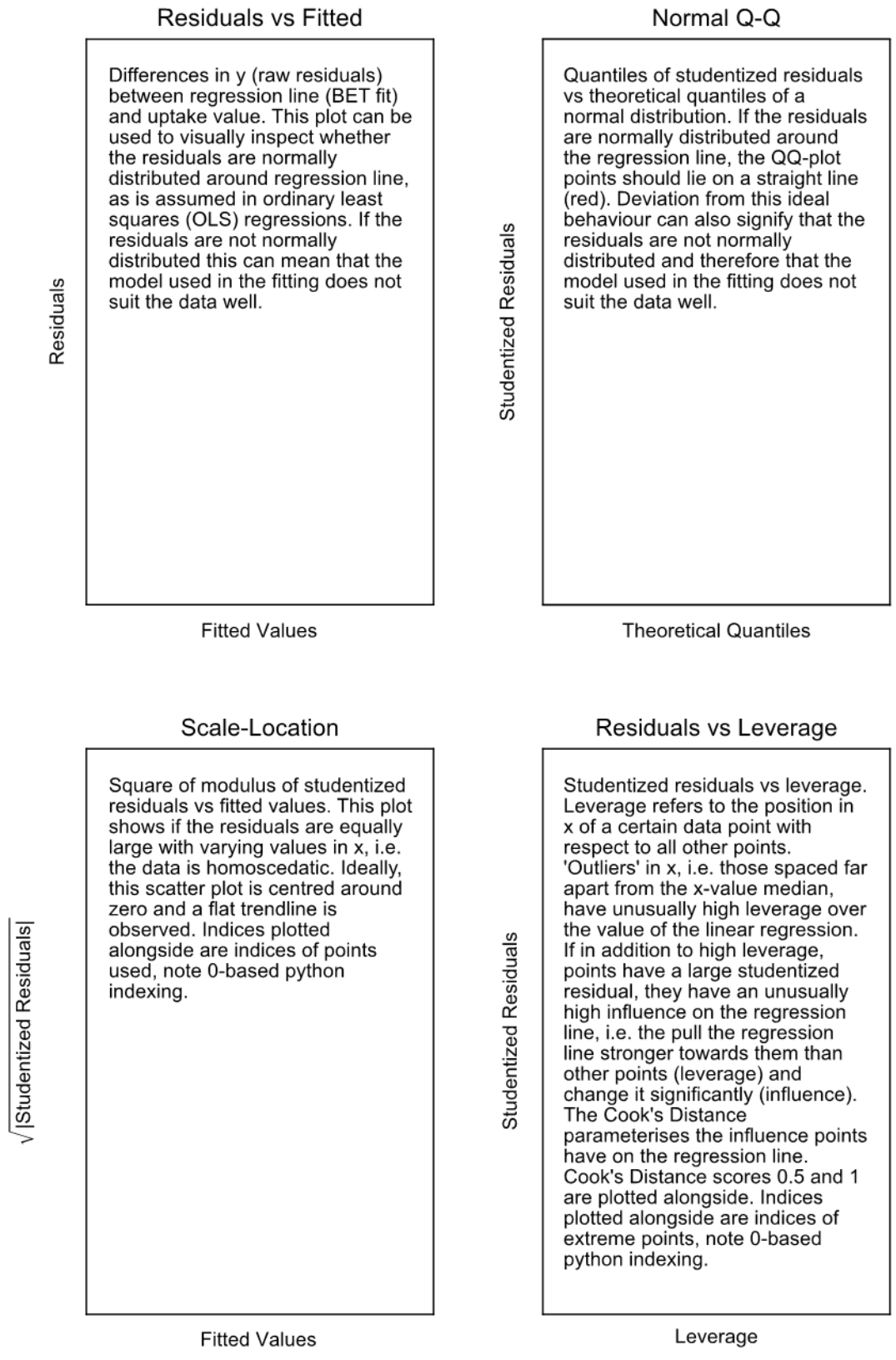

Figure S21 | Description of the different plots obtained in BETSI regression diagnostics.

0.000 acetonitrile fraction

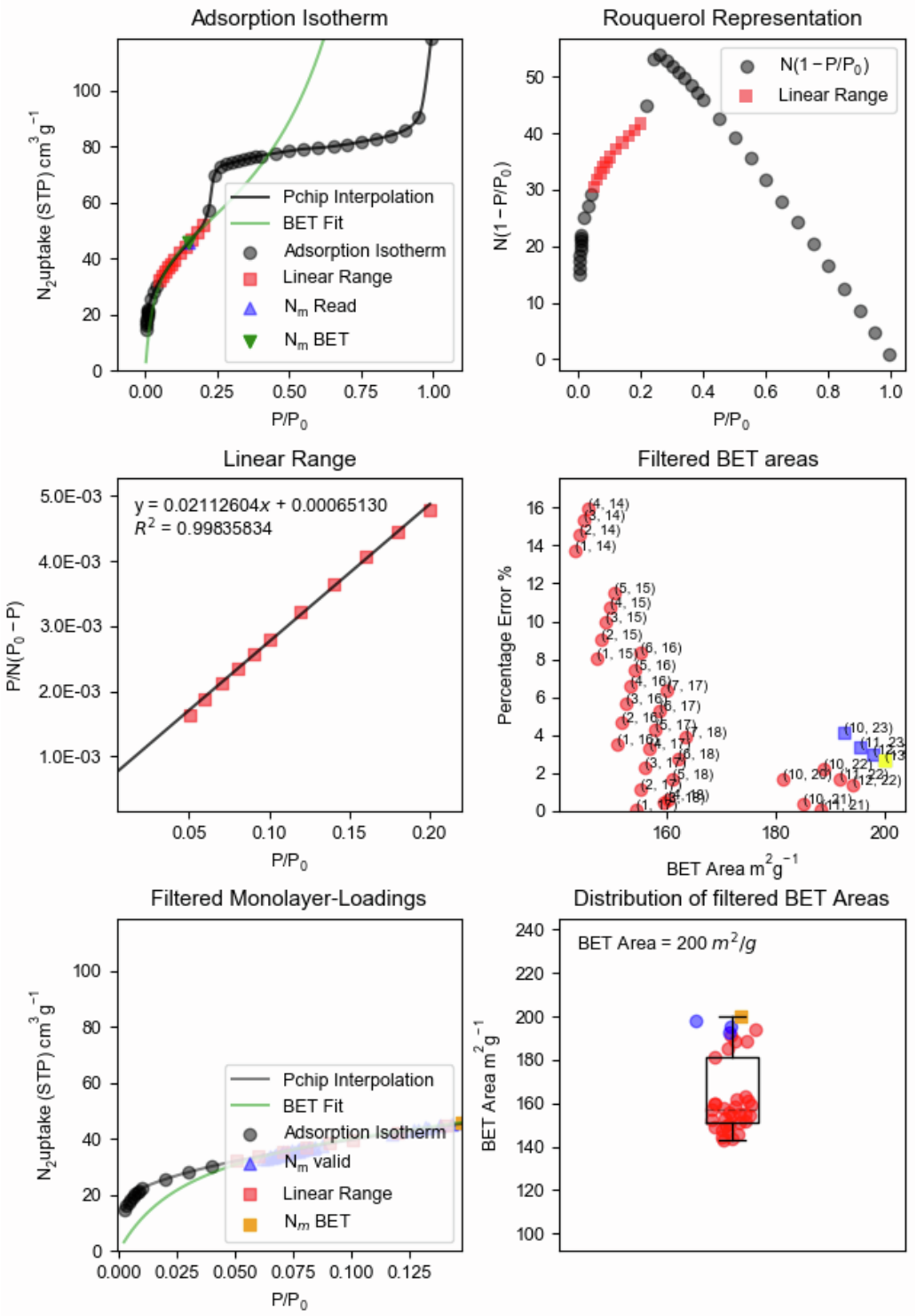

Figure S22 | BETSI analysis for 0.000 acetonitrile fraction sample.

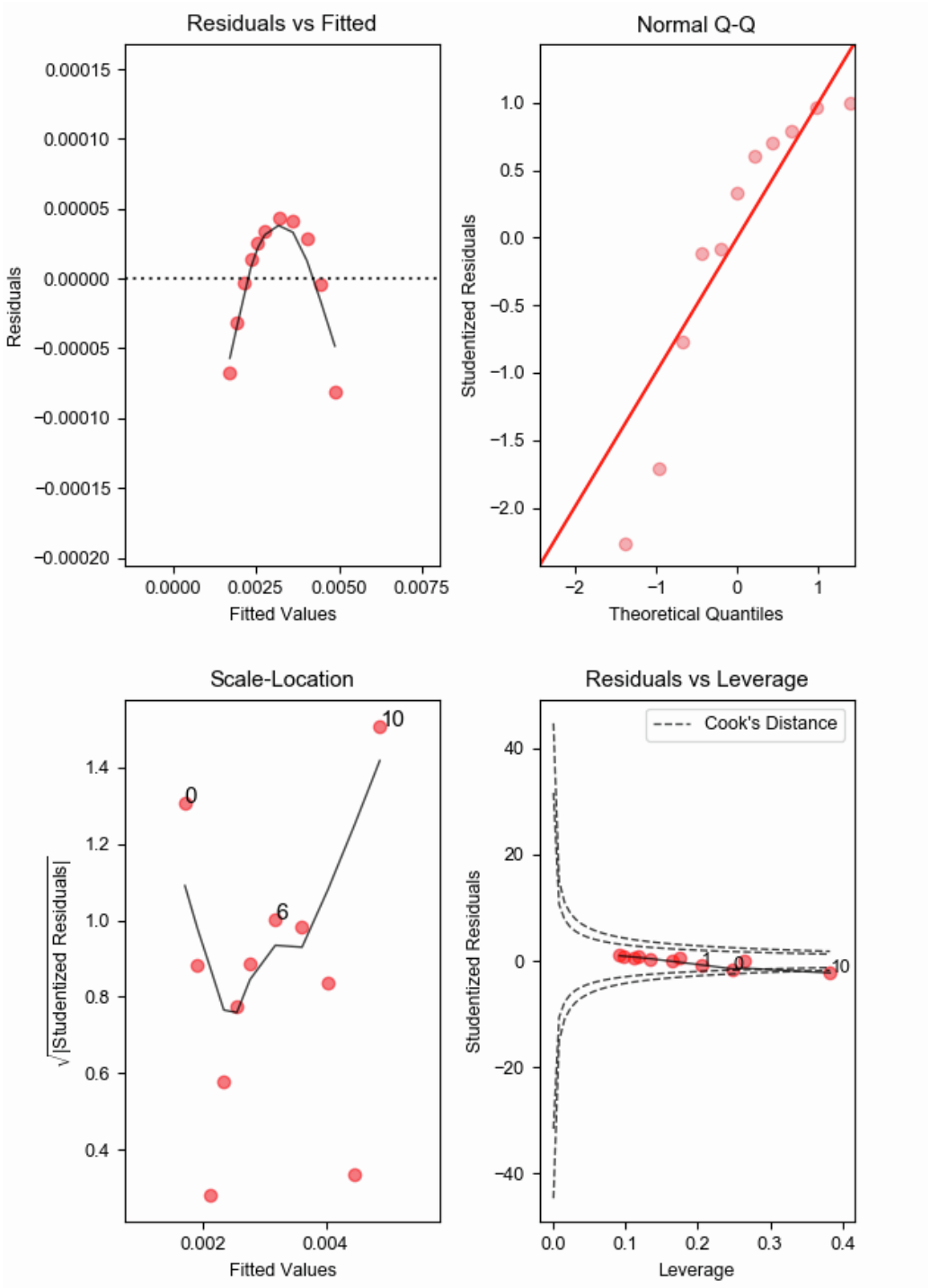

Figure S23 | BETSI regression diagnostics for 0.000 acetonitrile fraction sample.

0.250 acetonitrile fraction

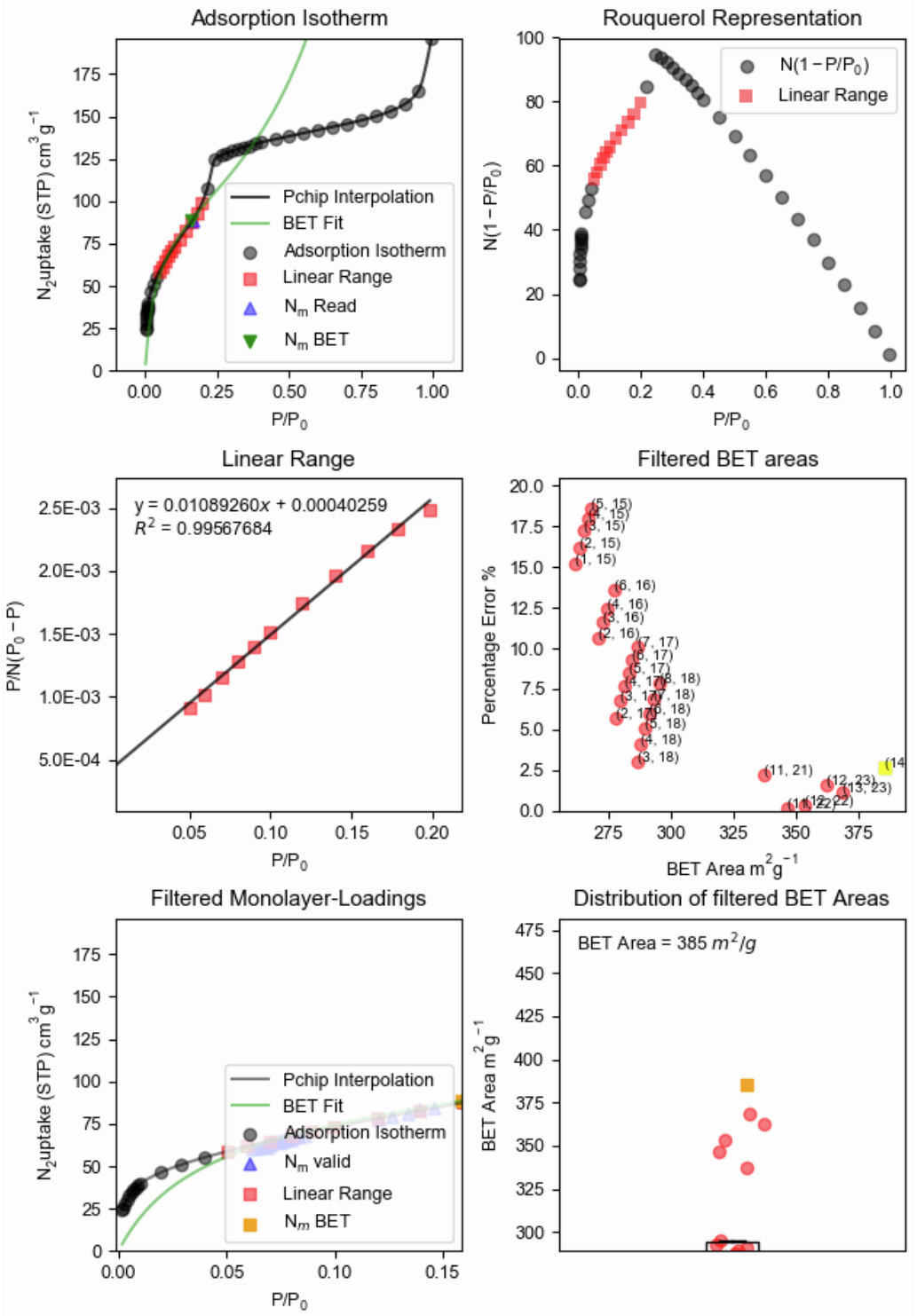

Figure S24 | BETSI analysis for 0.250 acetonitrile fraction sample.

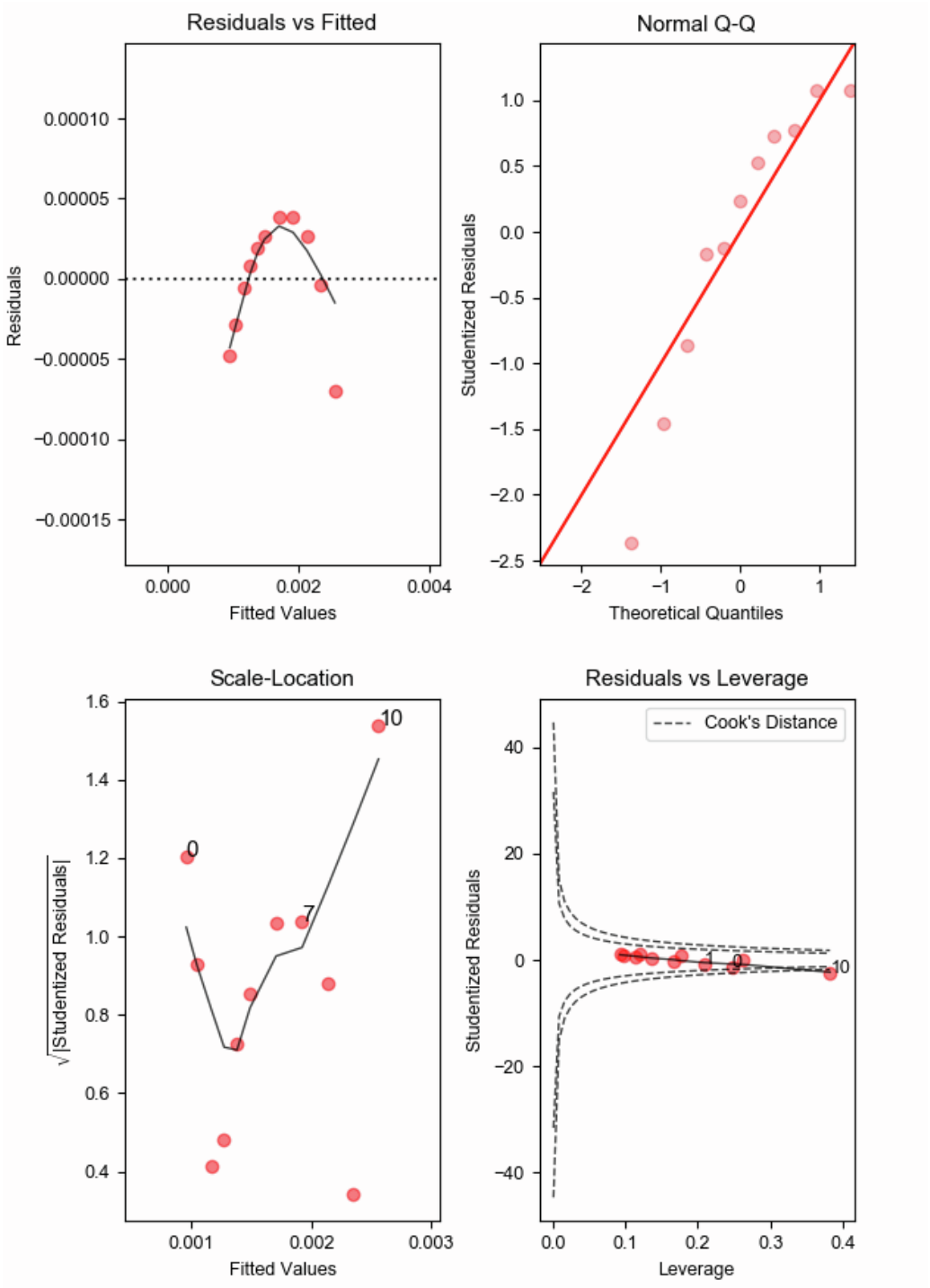

Figure S25 | BETSI regression diagnostics for 0.250 acetonitrile fraction sample.

0.500 acetonitrile fraction

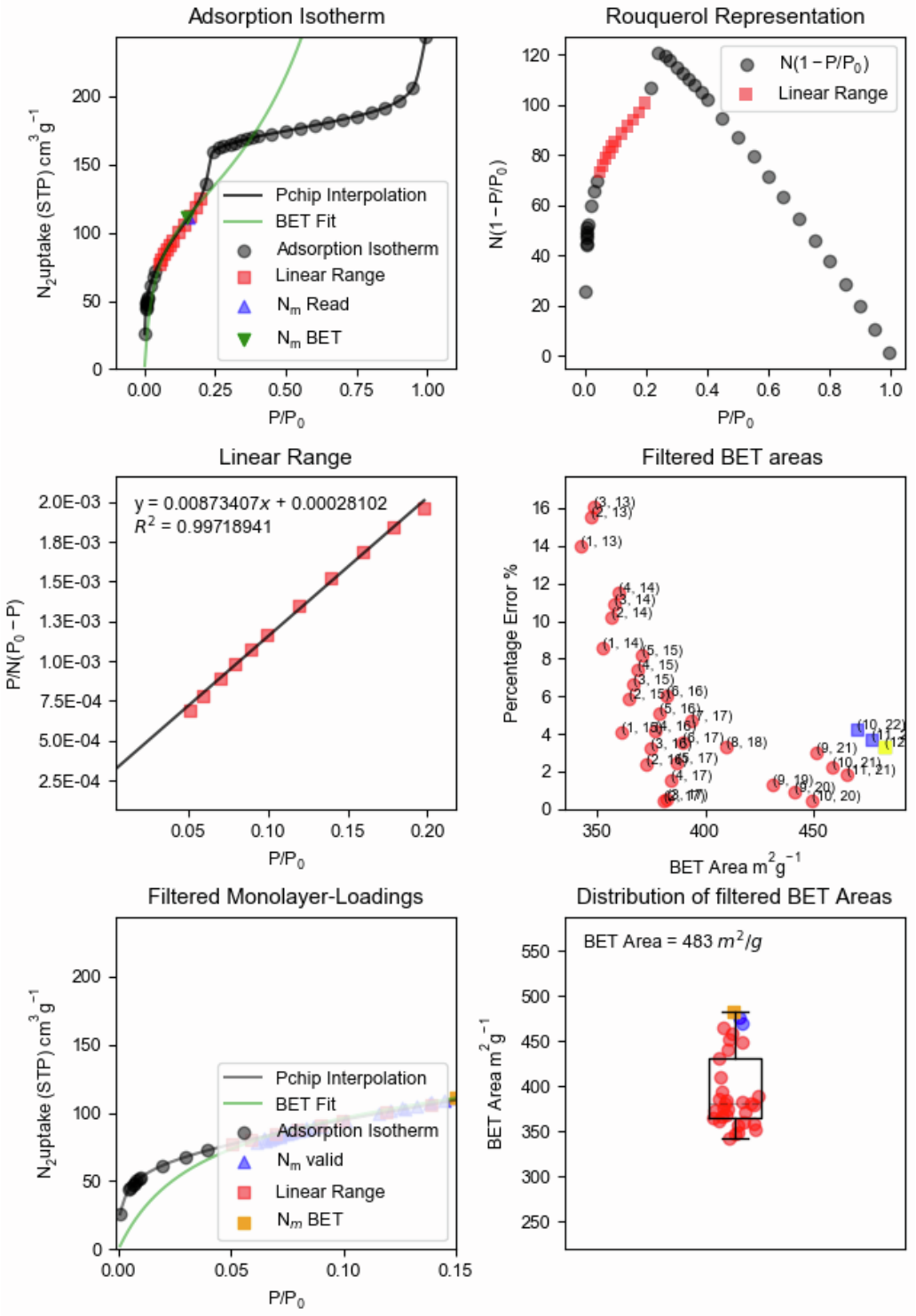

Figure S26 | BETSI analysis for 0.500 acetonitrile fraction sample.

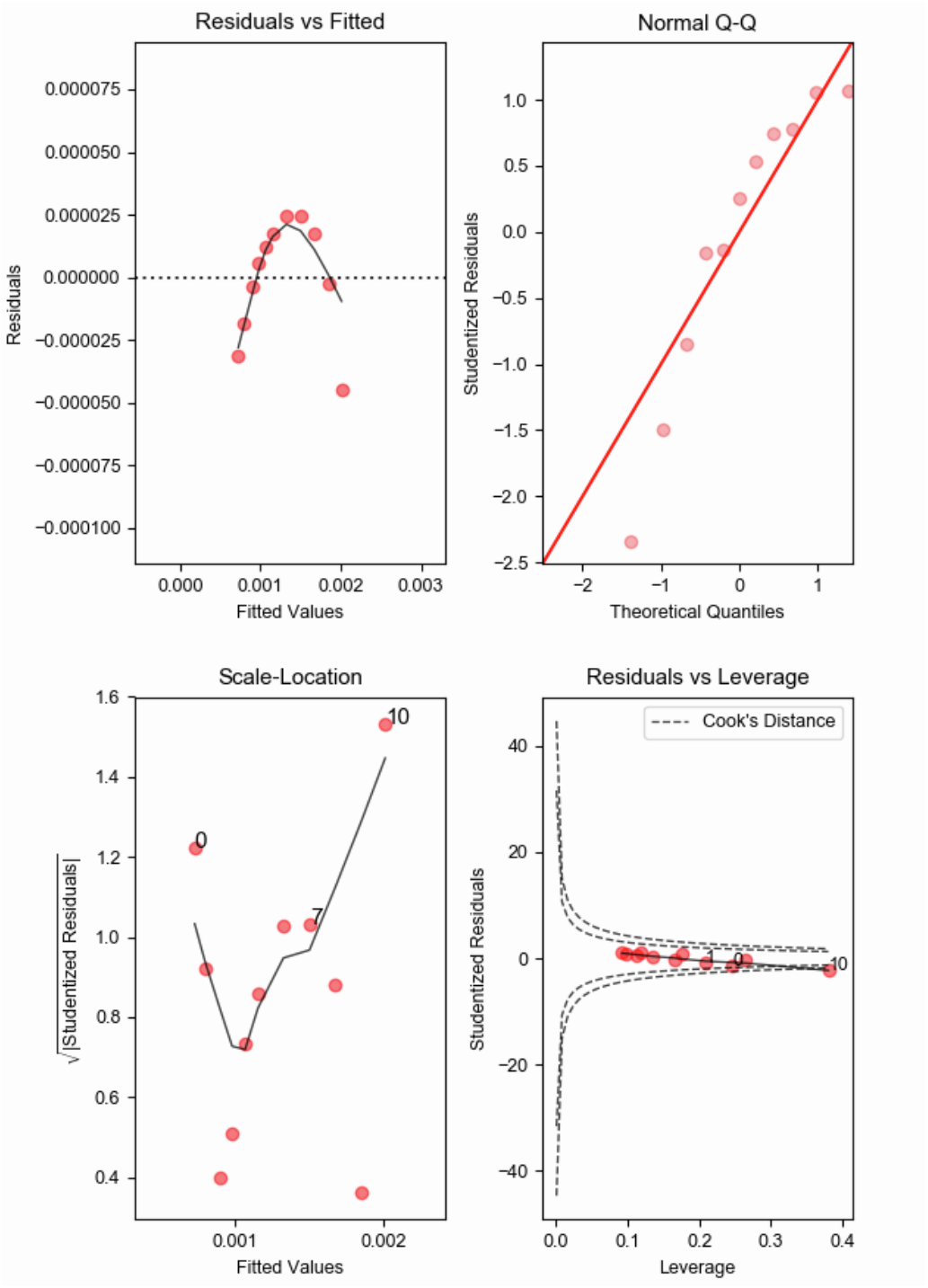

Figure S27 | BETSI regression diagnostics for 0.500 acetonitrile fraction sample.

0.668 acetonitrile fraction

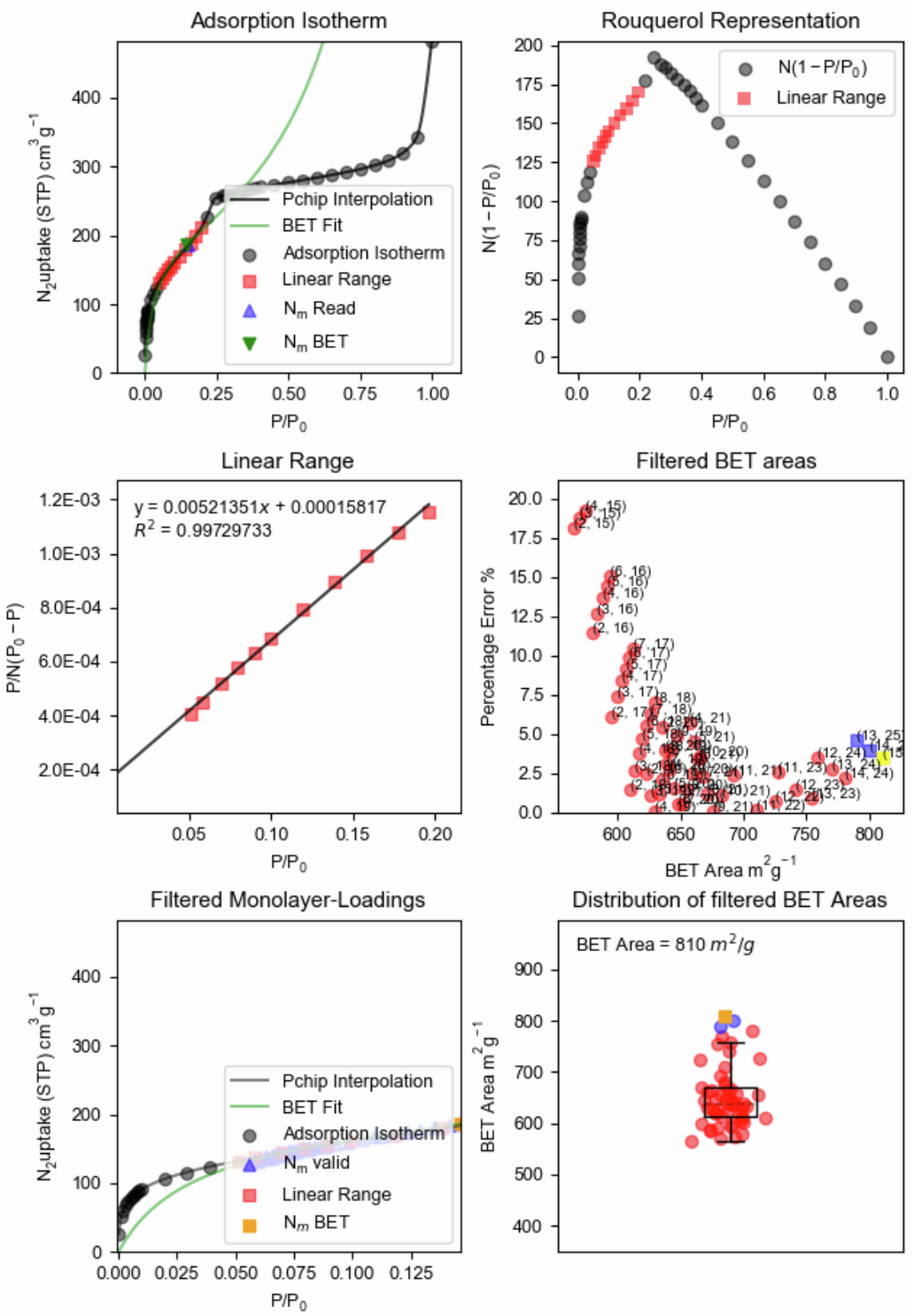

Figure S28 | BETSI analysis for 0.668 acetonitrile fraction sample.

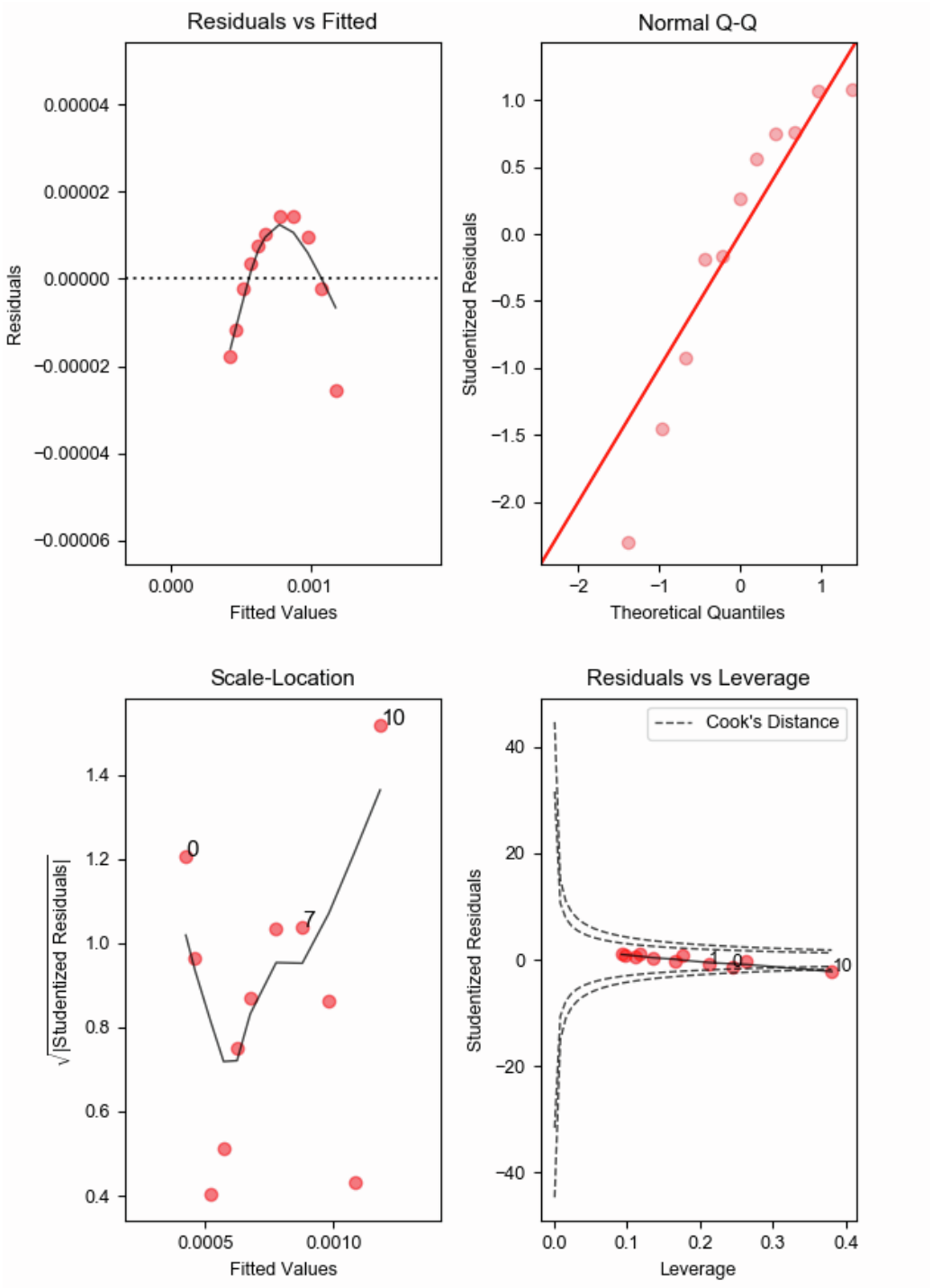

Figure S29 | BETSI regression diagnostics for 0.668 acetonitrile fraction sample.

0.750 acetonitrile fraction

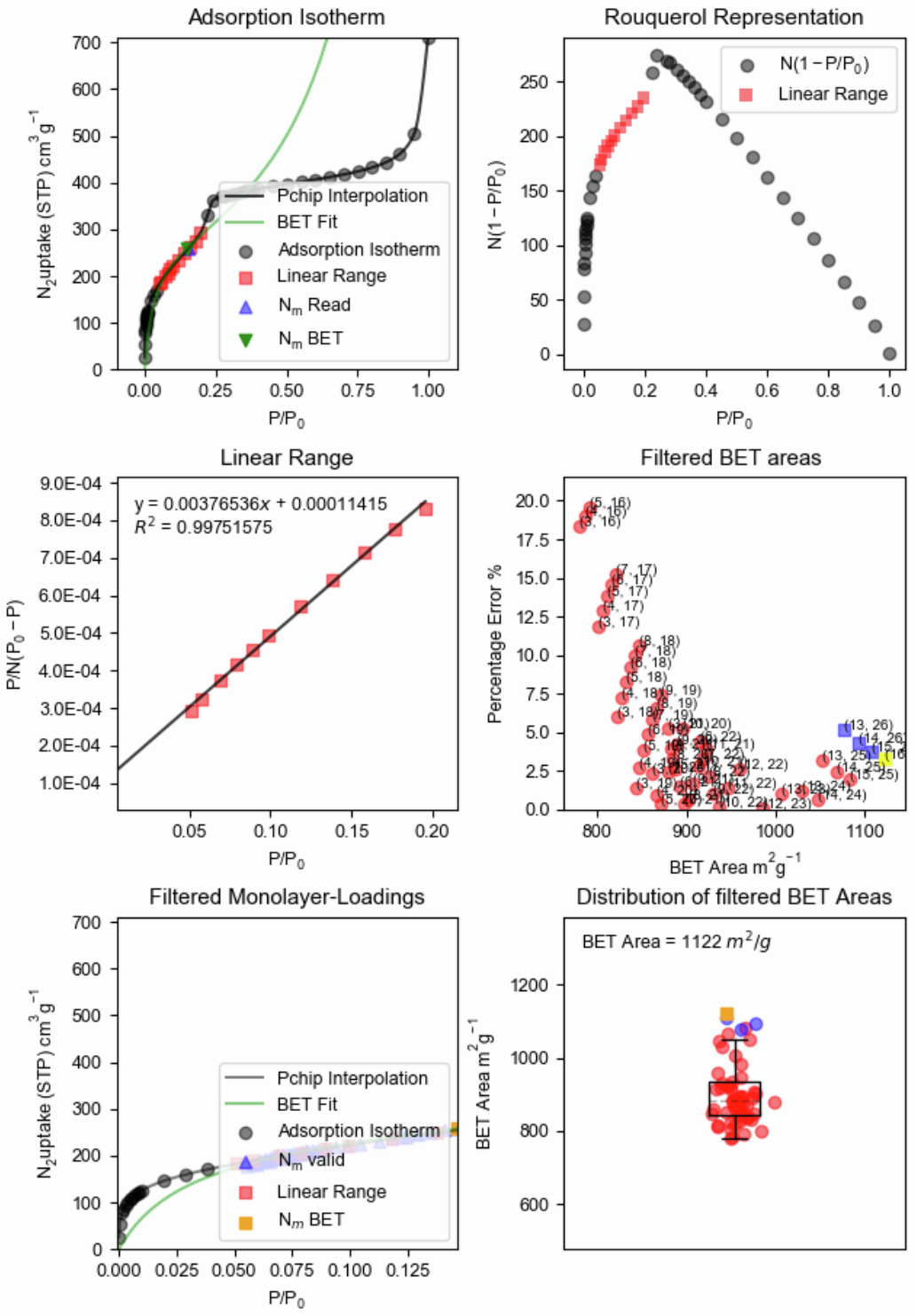

Figure S30 | BETSI analysis for 0.750 acetonitrile fraction sample.

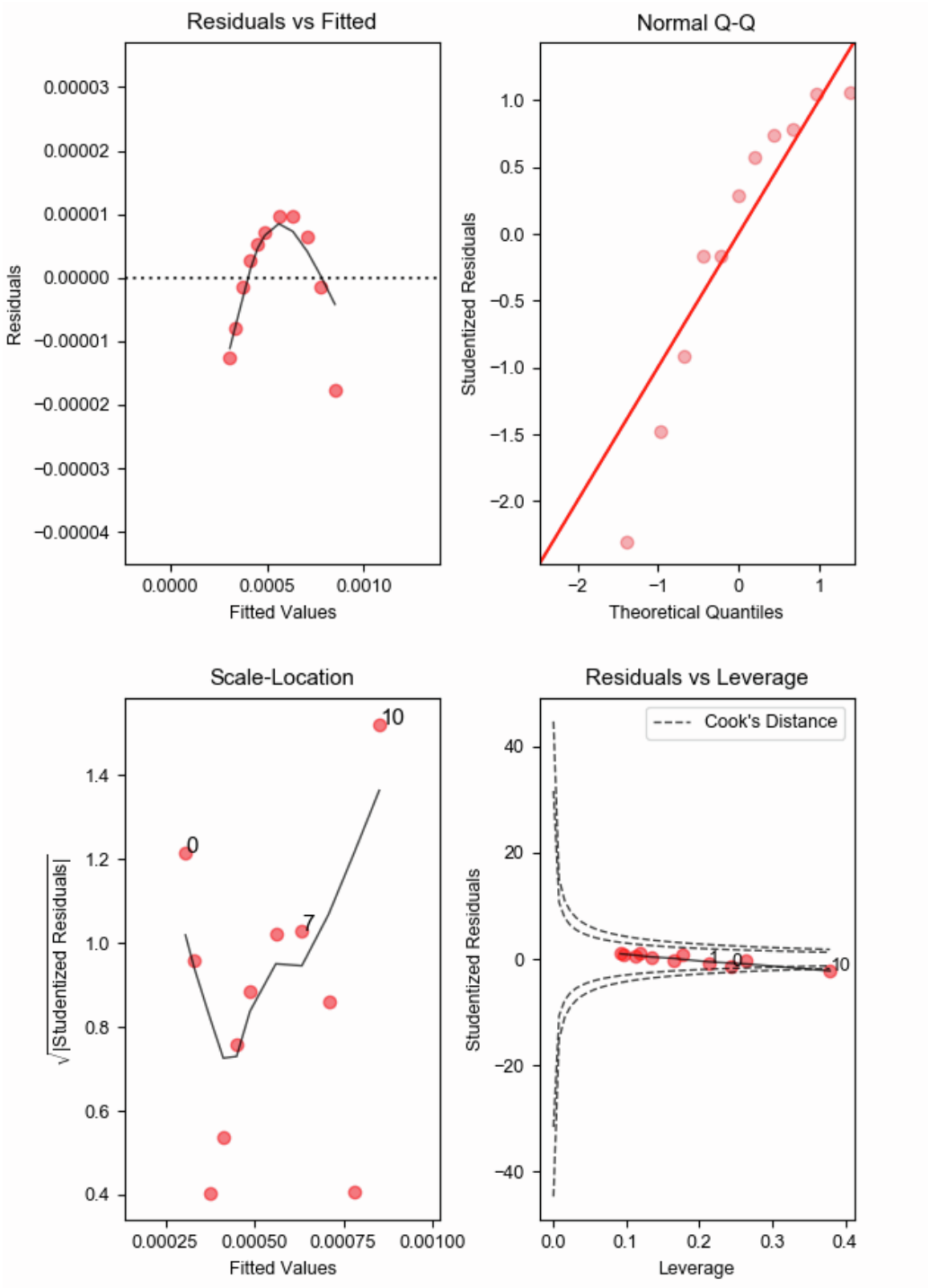

Figure S31 | BETSI regression diagnostics for 0.750 acetonitrile fraction sample.

0.775 acetonitrile fraction

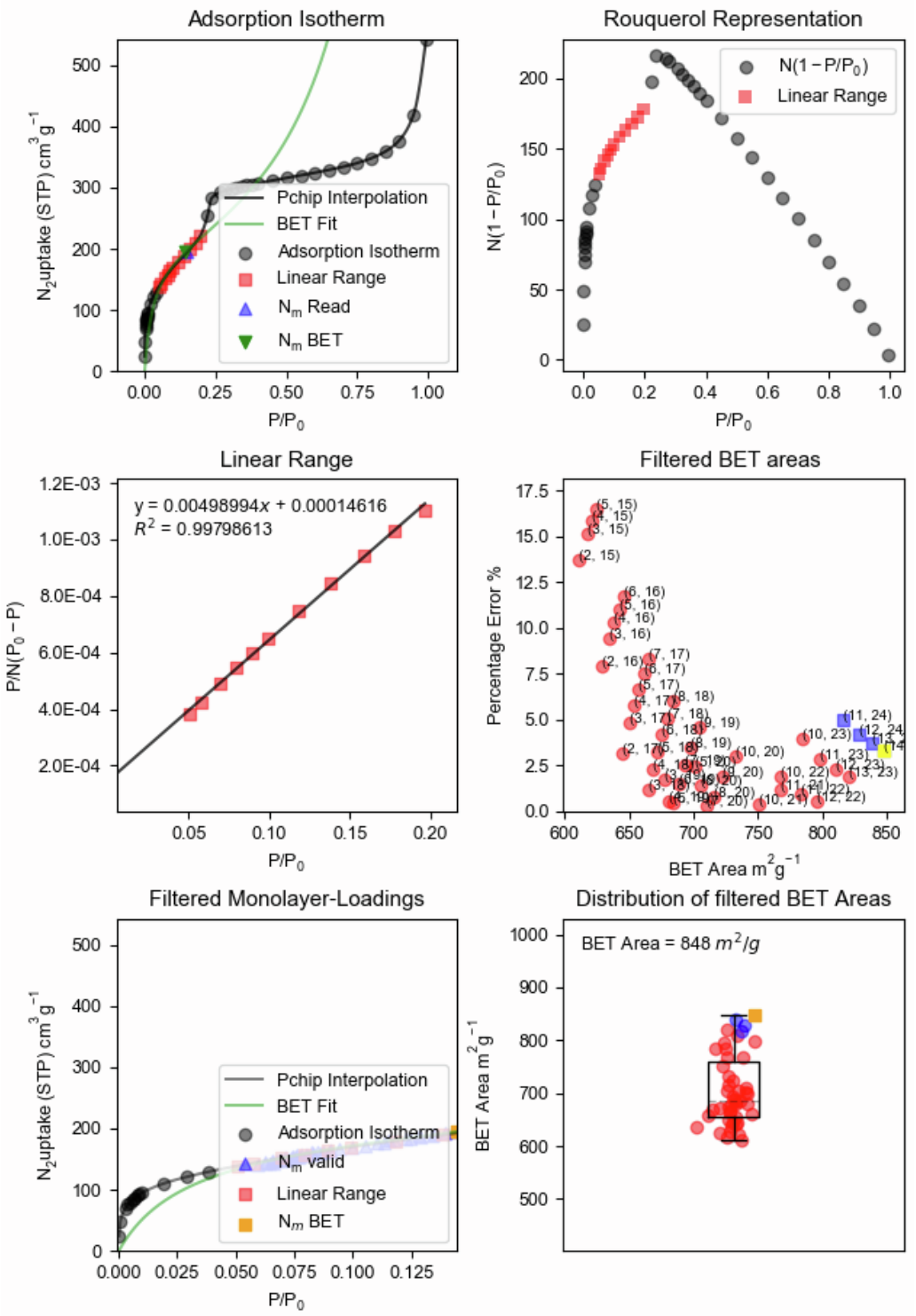

Figure S32 | BETSI analysis for 0.775 acetonitrile fraction sample.

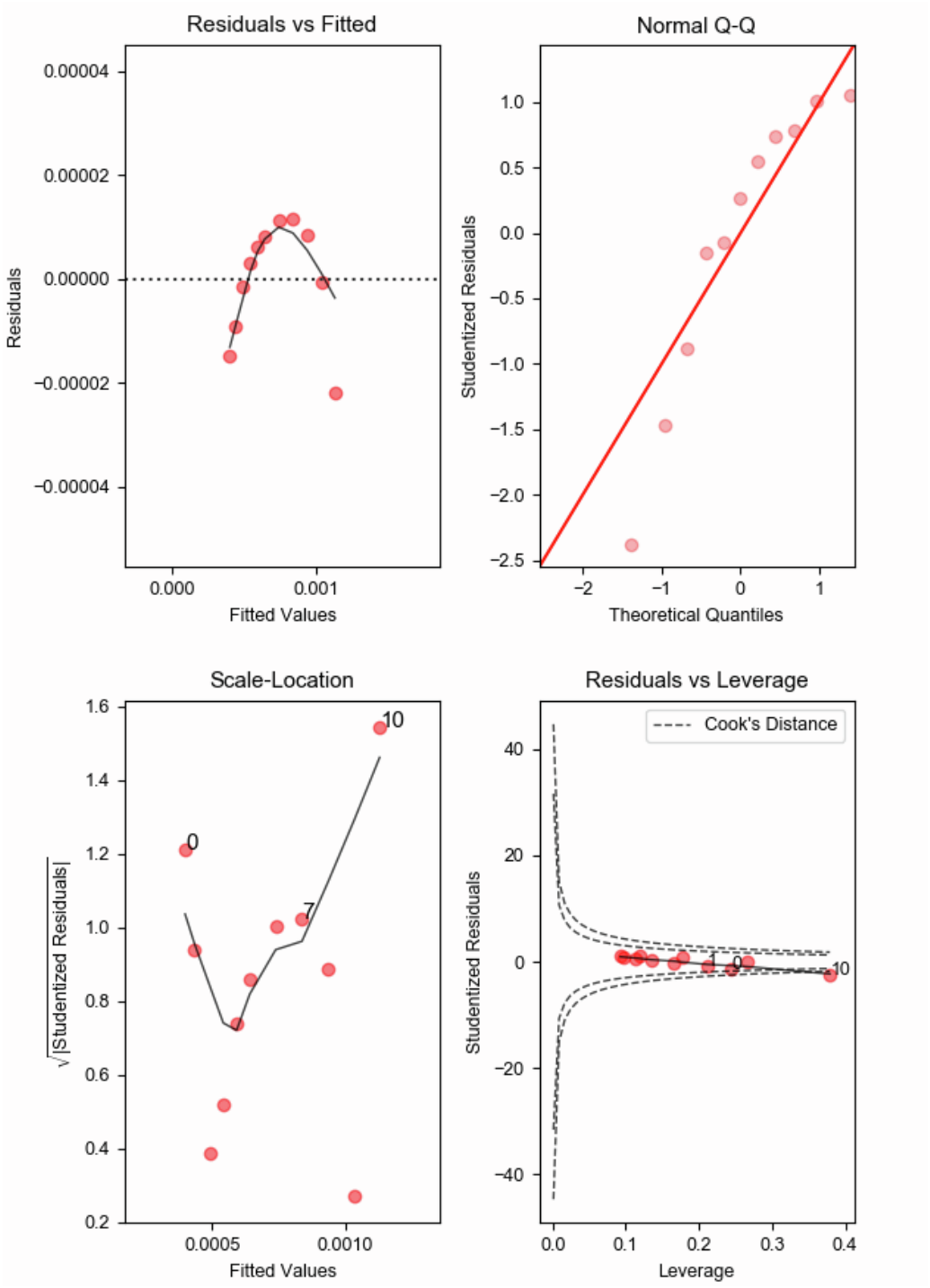

Figure S33 | BETSI regression diagnostics for 0.775 acetonitrile fraction sample.

0.833 acetonitrile fraction

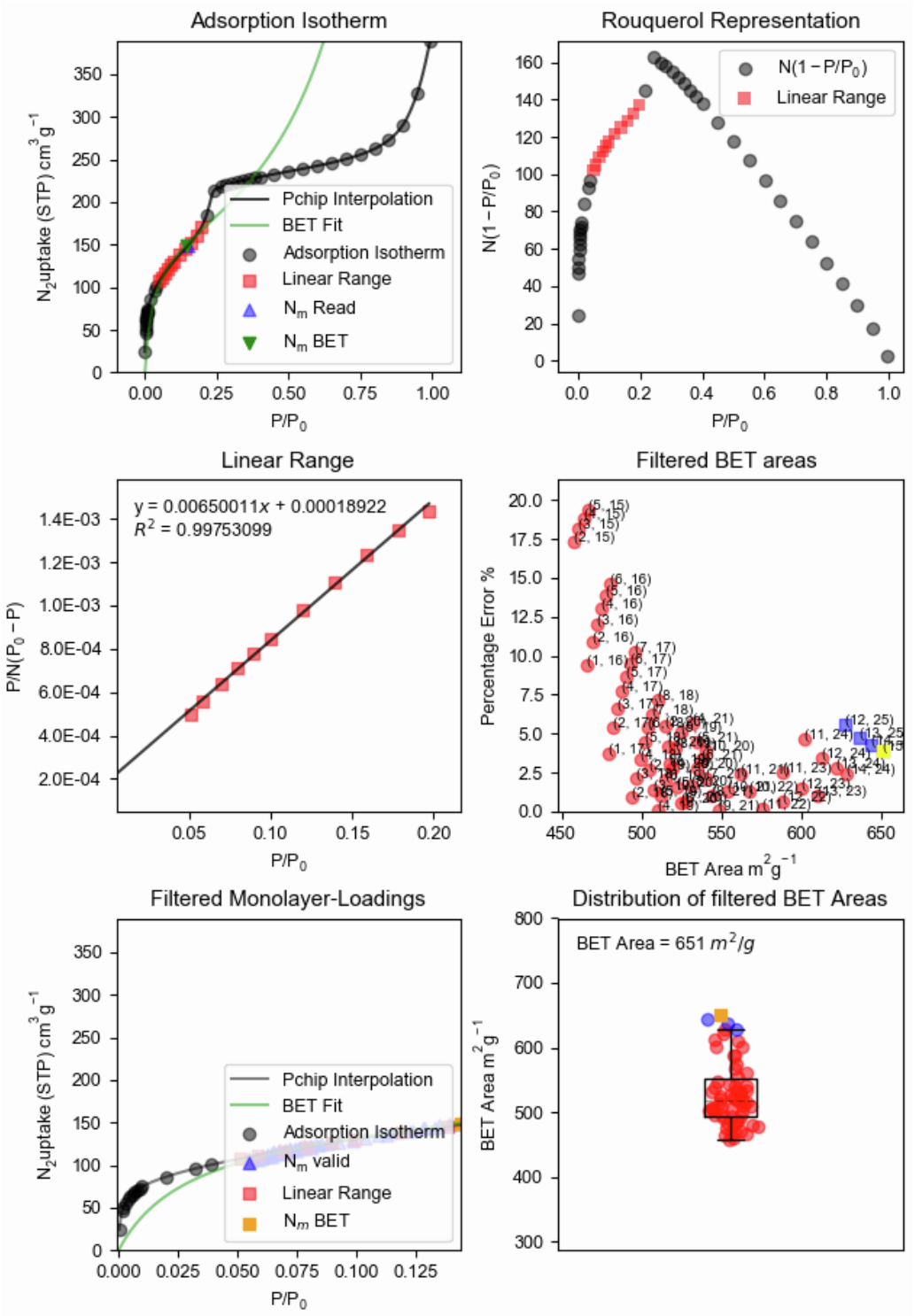

Figure S34 | BETSI analysis for 0.833 acetonitrile fraction sample.

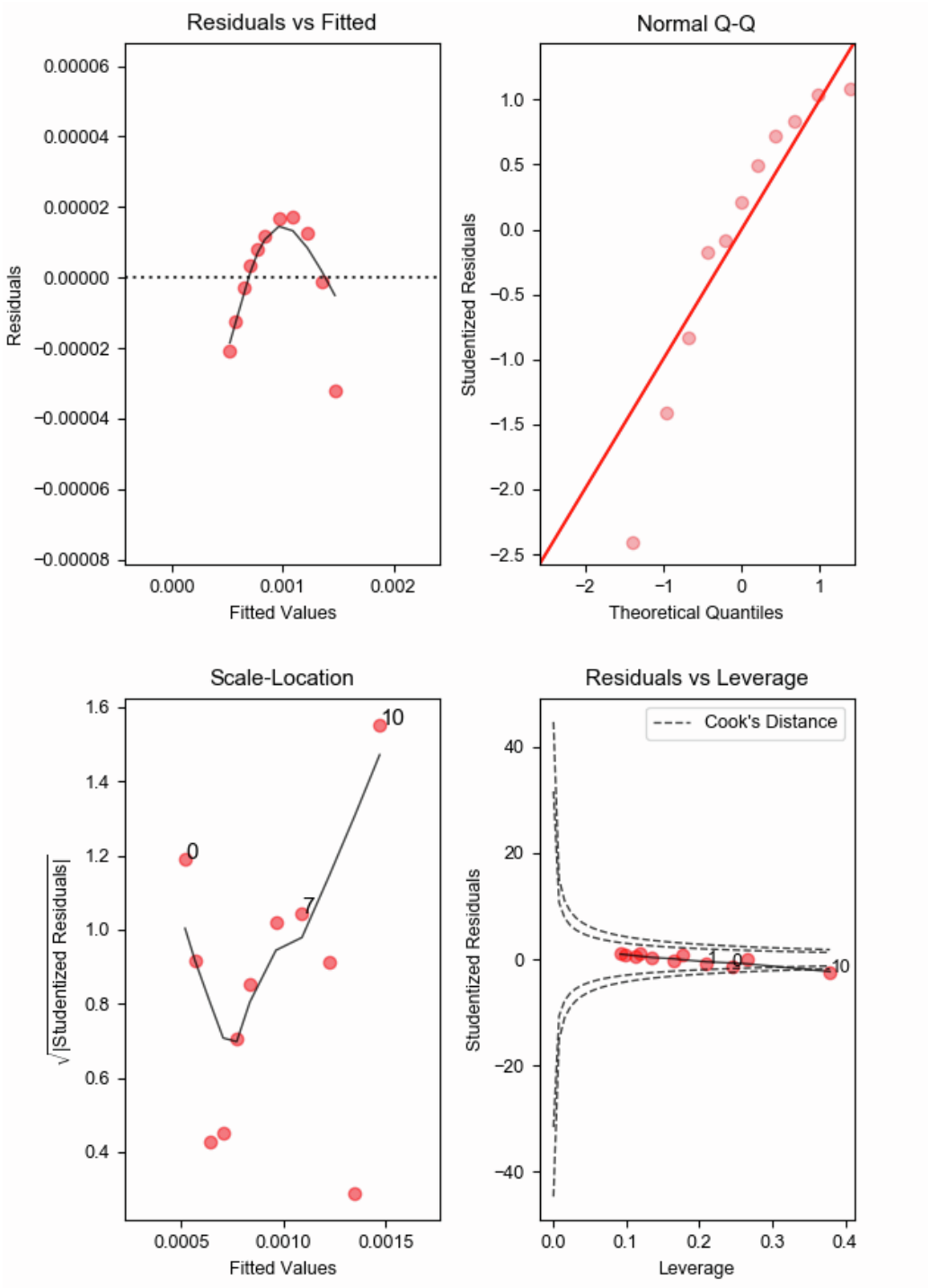

Figure S35 | BETSI regression diagnostics for 0.833 acetonitrile fraction sample.

1.000 acetonitrile fraction sample

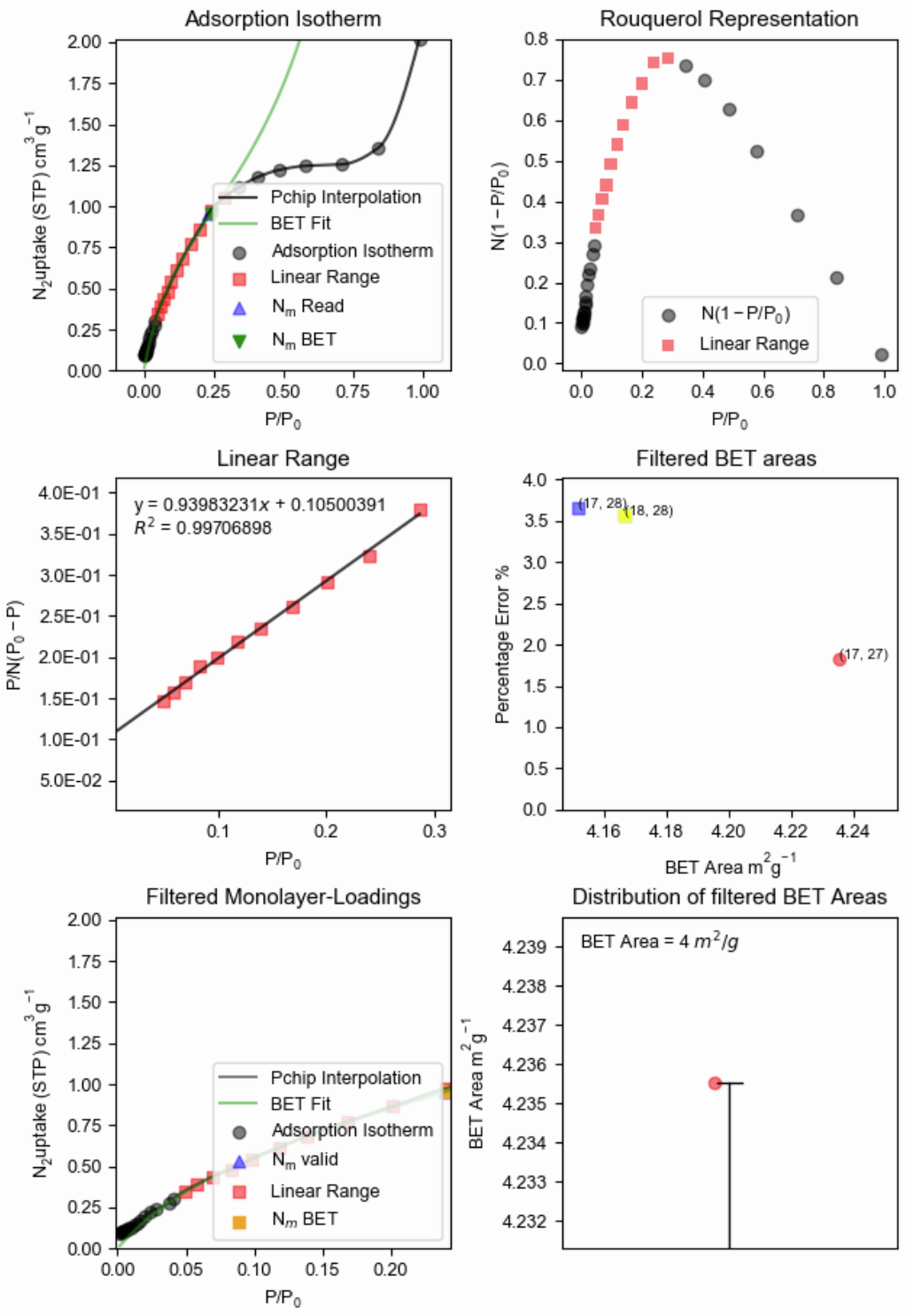

Figure S36 | BETSI analysis for 1.000 acetonitrile fraction sample.

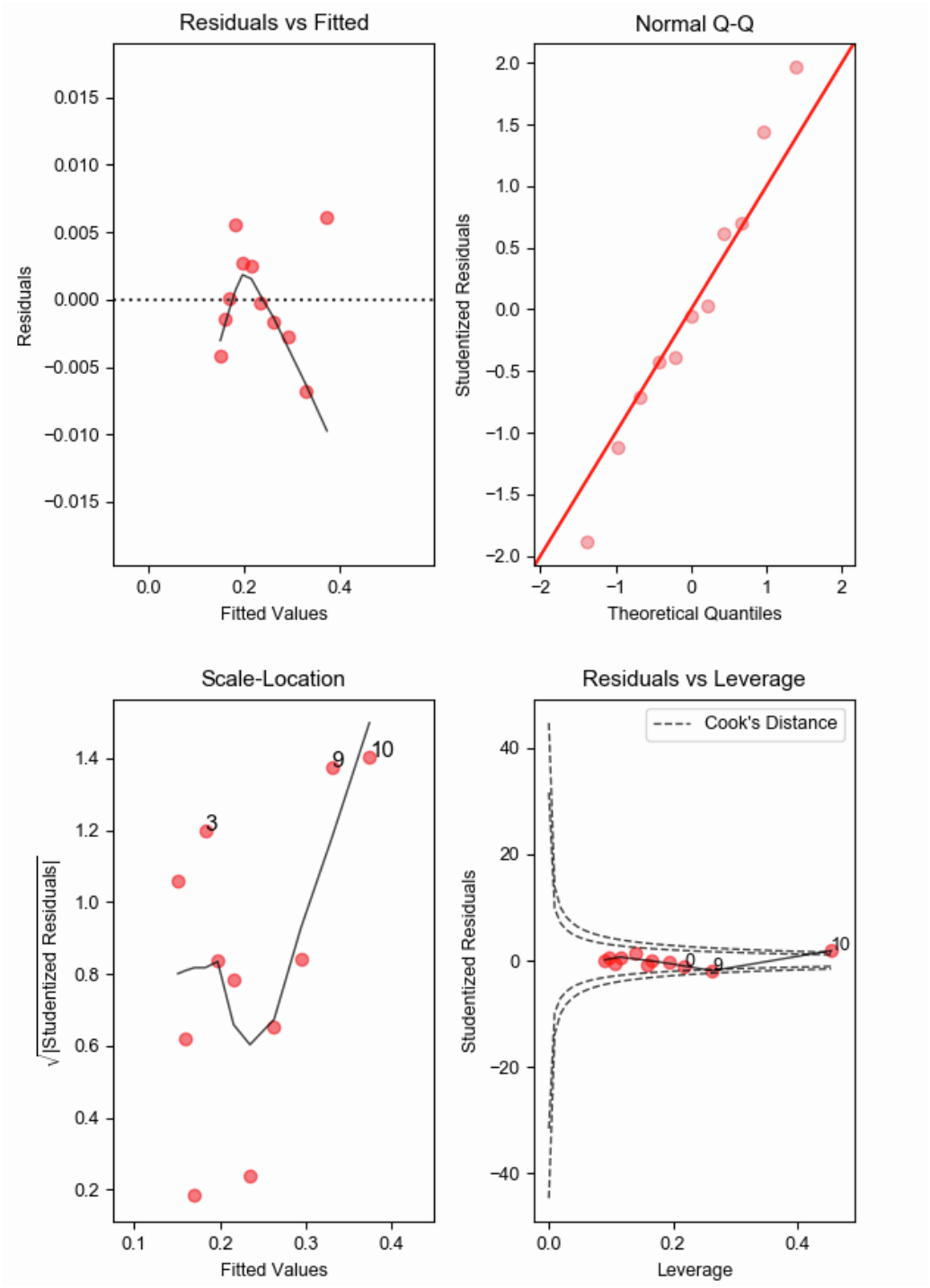

Figure S37 | BETSI regression diagnostics for 1.000 acetonitrile fraction sample.

1.000 acetonitrile fraction 3 bar h^{-1} $scCO_2$ activation

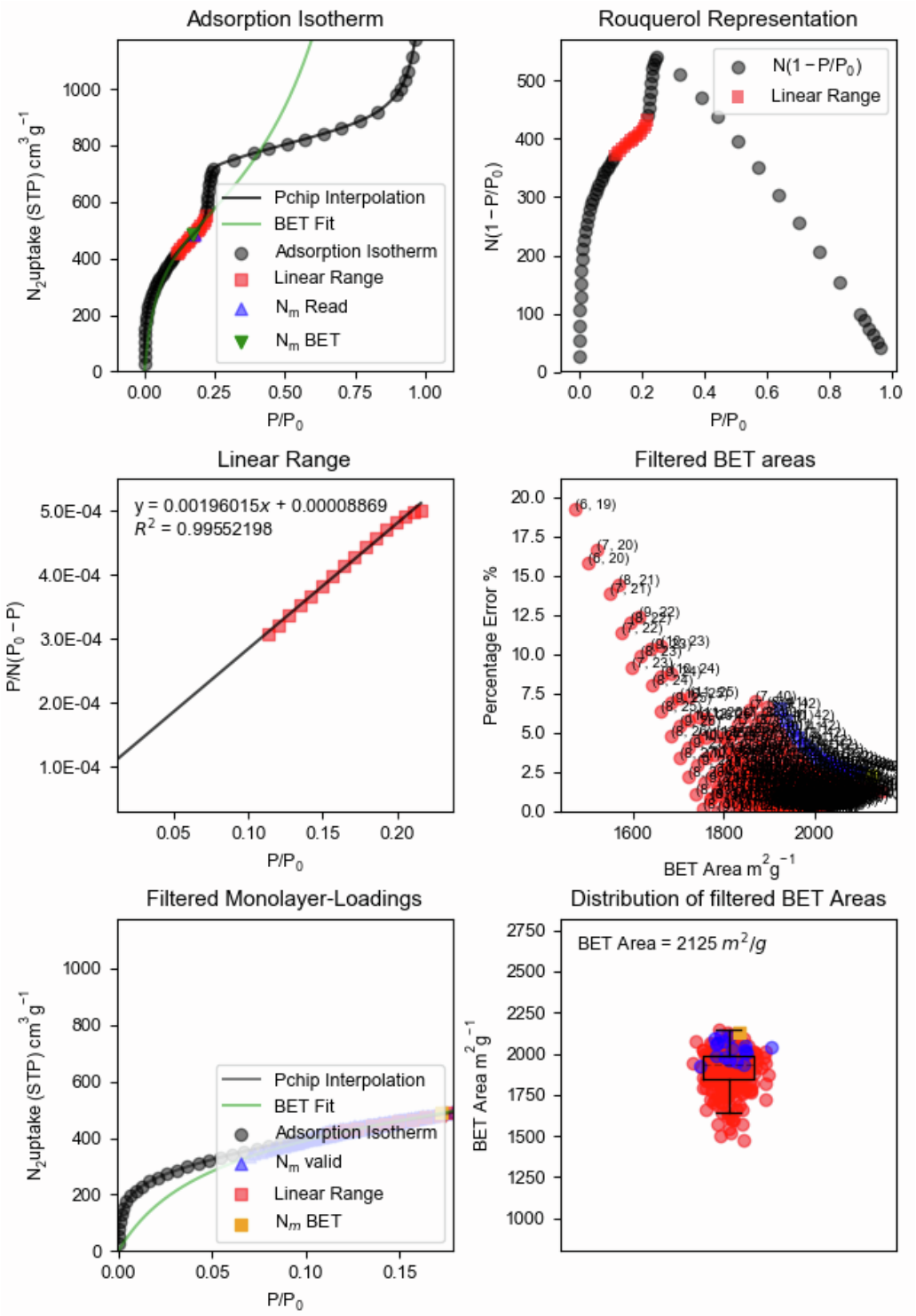

Figure S38 | BETSI analysis for 1.000 acetonitrile fraction 3 bar h^{-1} $scCO_2$ activation sample.

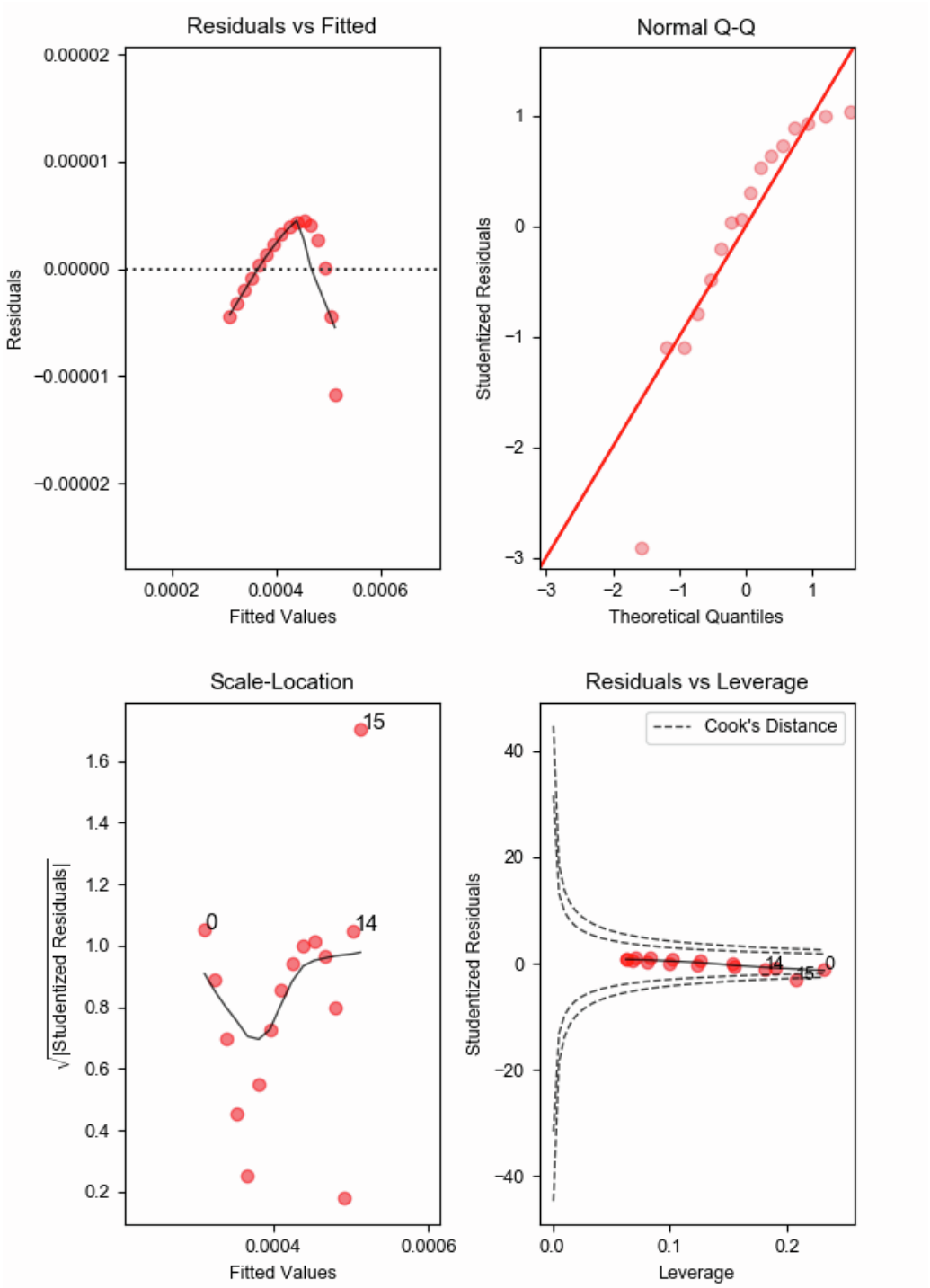

Figure S39 | BETSI regression diagnostics for 1.000 acetonitrile fraction 3 bar h^{-1} $scCO_2$ activation sample.

1.000 acetonitrile fraction 8 bar h^{-1} $scCO_2$ activation

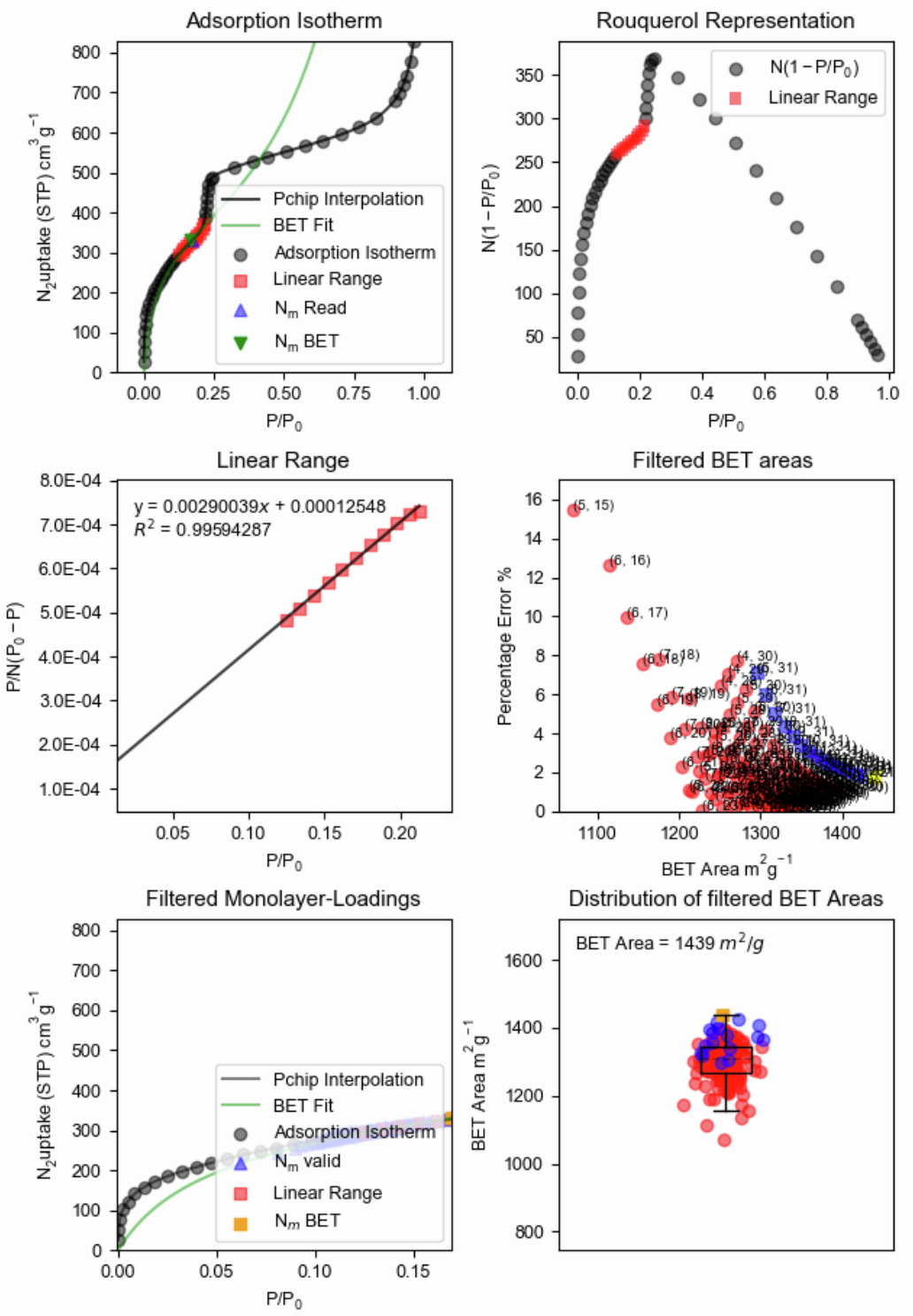

Figure S40 | BETSI analysis for 1.000 acetonitrile fraction 8 bar h^{-1} $scCO_2$ activation sample.

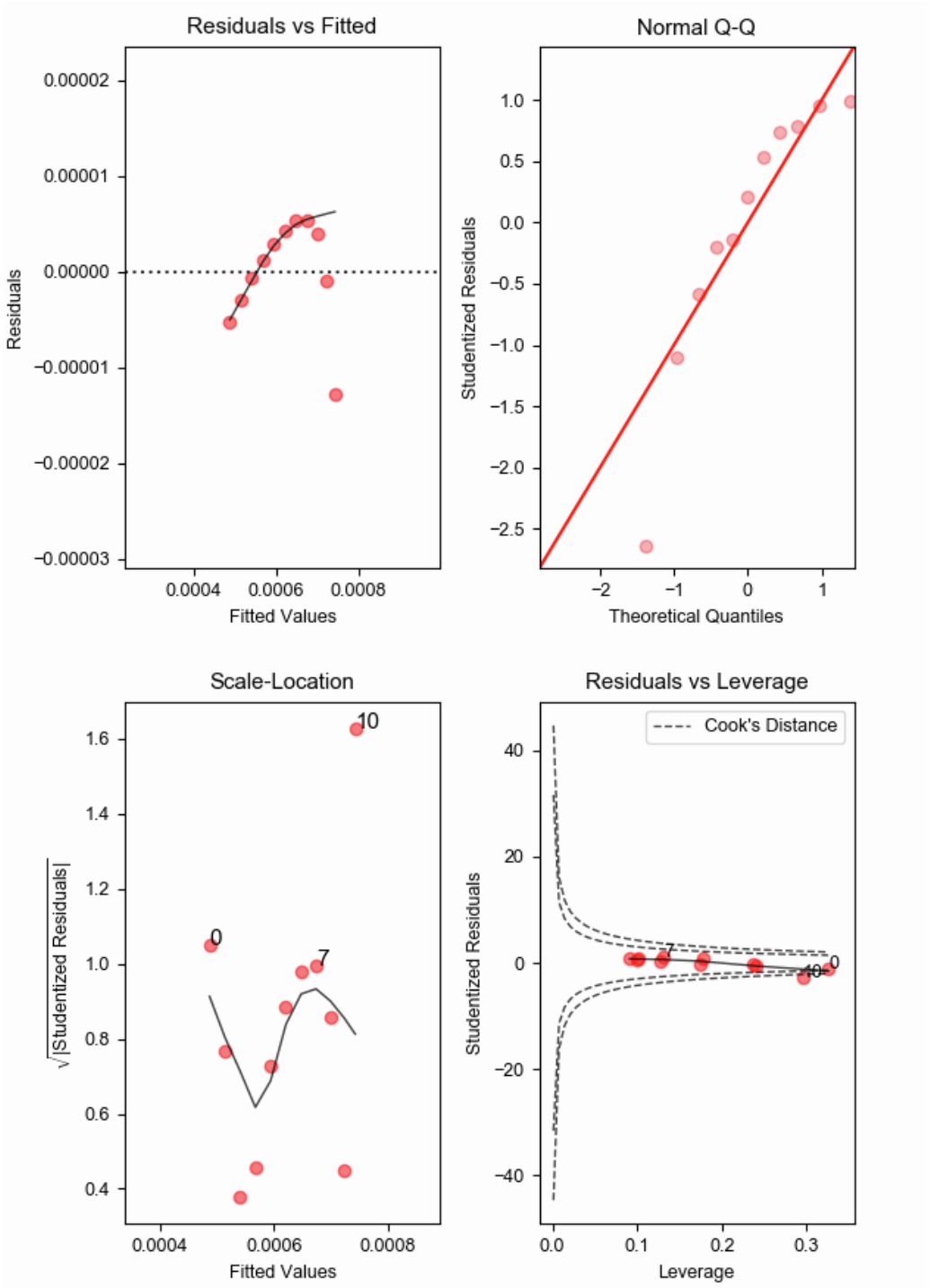

Figure S41 | BETSI regression diagnostics for 1.000 acetonitrile fraction 8 bar h^{-1} $scCO_2$ activation sample.

TPB-DMTP-COF powder

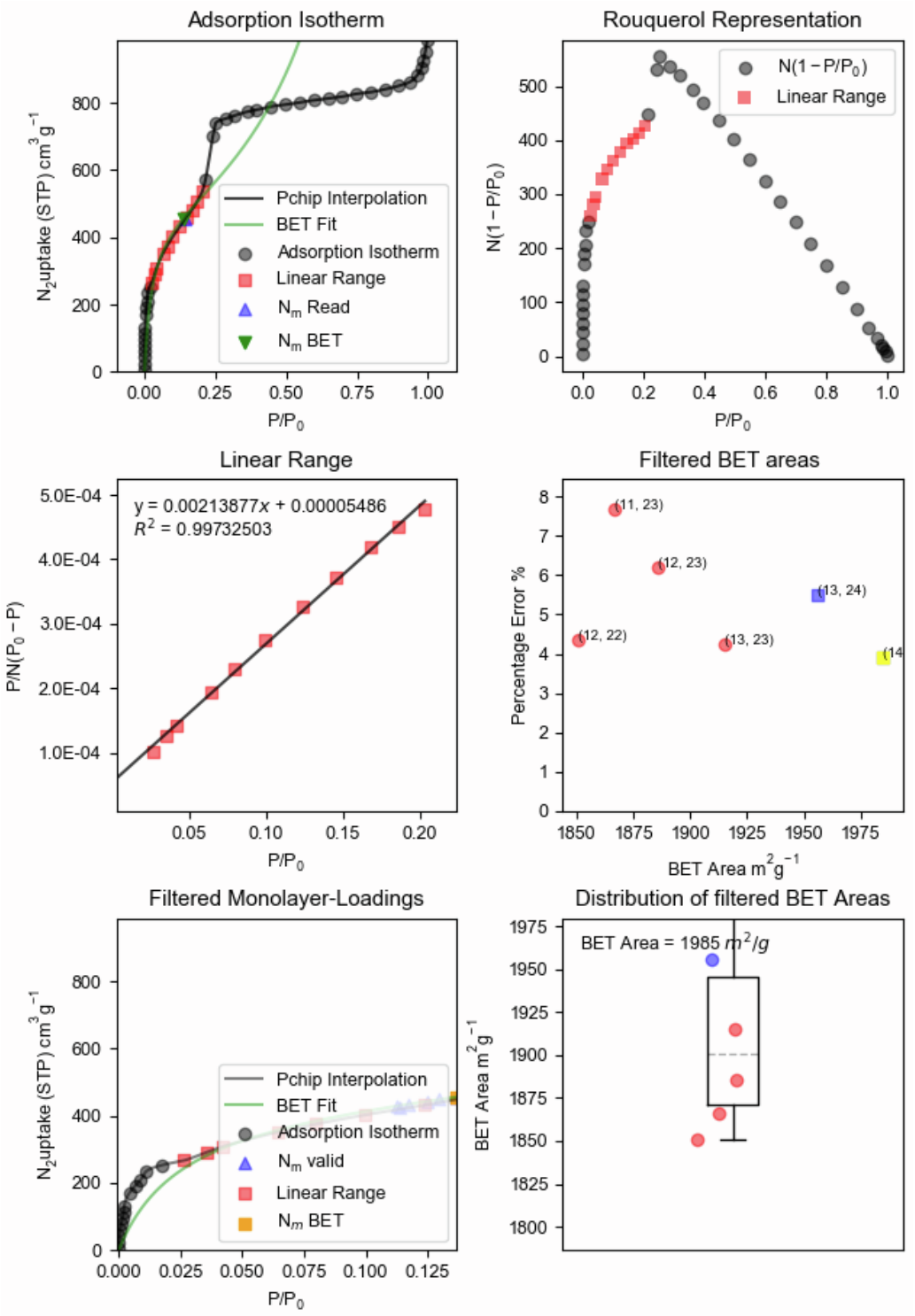

Figure S42 | BETSI analysis for TPB-DMTP-COF powder.

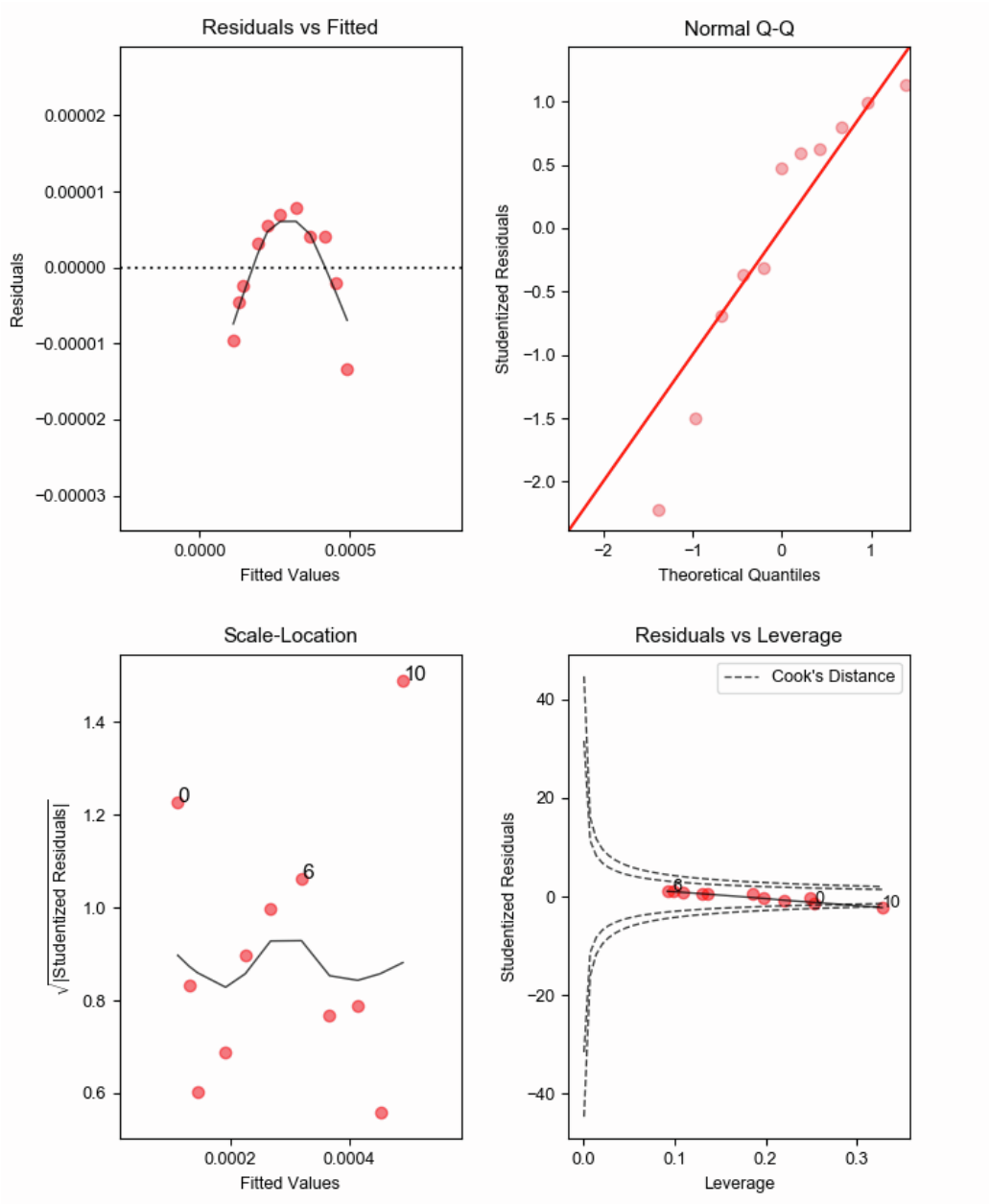

Figure S43 | BETSI regression diagnostics for TPB-DMTP-COF powder.

S10. Comparisons with literature

BET area, density, and mechanical properties

Table S6 | Comparison between TPB-DMTP-COF monolith and other monoliths/aerogels/pellets found in the literature.

Material	BET Area ($m^2 g^{-1}$)	Density (g cm^{-3})	Binder/Additive/High Pressure	Mechanical Properties	Ref.
TPB-DMTP-COF	2125	0.1558	✗	Indentation modulus = 3.71 ± 0.20 GPa. Hardness = 0.18 ± 0.02 GPa	This work
TFPT-HZ-COF	881.05	0.029	✓	Compressive strength = 8.69 kPa, compressed to 60% strain load	37
TPT-HZ-COF	174.86	0.04	✗	Compressive strength = 2.37 kPa, compressed to 60% strain load	37
TAPA-TFPA	186	0.031	✗	Compressive strength = 55.55 kPa, compressed to 70% strain load	38
TAPB-PDA	2273	0.026	✗	Compressive strength = 24.13 kPa, compressed to 70% strain load	38
TAPB-OMePDA	2258	0.032	✗	Compressive strength = 58.11 kPa, compressed to 70% strain load	38
TAPB-BrPDA	682	0.041	✗	Compressive strength = 20.63 kPa, compressed to 70% strain load	38
TAPB-TFPA	1626	0.036	✗	Compressive strength = 58.39 kPa, compressed to 70% strain load	38
BPDA-BTCA	1142	0.031	✗	**Not reported**	38
TAPB-BTCA-AGCOF	1146	0.0195	✗	Elastic modulus = E = 4070.4 Pa, $E_{specific}$ = 208.64 Pa m3/kg	39
PPDA-BTCA-AGCOF	677	0.0208	✗	Elastic modulus = E = 1771.3 Pa, $E_{specific}$ = 85.33 Pa m3/kg	39
TAPB-PDA-AGCOF	2535	0.0173	✗	Elastic modulus = E = 769.85 Pa, $E_{specific}$ = 44.48 Pa m3/kg	39
M_{BTCA} (TAPB-BTCA-COF)	535	0.74	✓	Tablet press with 20 bar pressure was used to create the monolith. Young's modulus (E) = 263 MPa and compressive strength = 45 MPa	40
COF/rGO	246	0.007	✓	COFs are grown in-situ along the surface of the 2D graphene sheets. Compressive stress=6.88 kPa, compressed to 50 % compressive strain	41
COF-GO Foam 1	971	**Not reported**	✓	Automatic Young's Modulus = 0.259 MPa. Compressive stress at maximum load = 0.034 MPa.	42
COF-GO Foam 2	500	**Not reported**	✓	**Not reported**	42
COF-GO Foam 3	624	**Not reported**	✓	**Not reported**	42
COF aerogel	2096.3	**Not reported**	✗	Compressive stress = 0.577 Mpa, compressed to 40 % compressive strain	43
COF-IL@chitosan	103.3	0.032–0.035	✓	Fabricated by chemical crosslinking of an allyl imidazolium ionic liquid-decorated COF (COF-IL) with a thiol-attached chitosan (chitosan–SH) binder via a photoinduced thiol–ene reaction. Compressive strength = 13.8 MPa, compressed to 75 % compressive strain	44
M43	105	**Not reported**	✓	Additive: Fresh prepolymerization solution containing the following, (1) polytheylenimine (PEI, M_n=1200), (2) octaglycidyldimethylsilyl POSS (POSS-expoxy), (3) polyethyleneglycol (PEG, M_n=10000), (4) 1-propanol, and (5) 1,4 - butanediol + 43 wt. % COF powder. Modulus of elasticity = 3.14 MPa	45
M28	281	**Not reported**	✓	Additive: Fresh prepolymerization solution containing the following, (1) polytheylenimine (PEI, M_n=1200), (2) octaglycidyldimethylsilyl POSS (POSS-expoxy), (3) polyethyleneglycol (PEG, M_n=10000), (4) 1-propanol, and (5) 1,4 - butanediol + 28 wt. % COF powder. Modulus of elasticity = 5.33 MPa	45
M16	154	**Not reported**	✓	Additive: Fresh prepolymerization solution containing the following, (1) polytheylenimine (PEI, M_n=1200), (2) octaglycidyldimethylsilyl POSS (POSS-expoxy), (3) polyethyleneglycol (PEG, M_n=10000), (4) 1-propanol, and (5) 1,4 - butanediol + 16 wt. % COF powder. Modulus of elasticity = 9.17 MPa	45

Separation performance

Table S7 | Selected performance values for monolithic materials in 15% CO_2 / 85% N_2 separations.

Material	BET Area ($m^2 g^{-1}$)	Density (g cm^{-3})	Binder/Additive/High Pressure	IAST Selectivity (1 bar; 298 K)	Breakthrough studies	Ref.
TPB-DMTP-COF	2125	0.1558	✗	12.4	✓	This work
SNW-1	794	Not reported	✗	66.5	✗	46
$_{mono}$UiO-66	1066	1.05	✗	28	✓	47
$_{mono}$HKUST-1	1603	1.06	✗	23	✓	47
$_{mono}$UiO-66-NH_2	1533	1.25	✗	30	✓	47

Table S8 | Selected performance values for monolithic materials in 50% CO_2 / 50% CH_4 separations.

Material	BET Area ($m^2 g^{-1}$)	Density (g cm^{-3})	Binder/Additive/High Pressure	IAST Selectivity (1 bar; 298 K)	Breakthrough studies	Ref.
TPB-DMTP-COF	2125	0.1558	✗	3.5	✓	This work
$_{mono}$UiO-66	1066	1.05	✗	36	✓	47
$_{mono}$HKUST-1	1603	1.06	✗	12	✓	47
$_{mono}$UiO-66-NH_2	1533	1.25	✗	54	✓	47
MIL-53 (Al, PVA)	Not reported	Not reported	✓	7	✓	48

S11. References

1. Ongari, D., Yakutovich, A. V., Talirz, L., and Smit, B. (2019). Building a Consistent and Reproducible Database for Adsorption Evaluation in Covalent–Organic Frameworks. ACS Cent. Sci. *5*, 1663-1675.
2. Dubbeldam, D., Calero, S., Ellis, D. E., and Snurr, R. Q. (2016). RASPA: molecular simulation software for adsorption and diffusion in flexible nanoporous materials. Mol. Simulat. *42*, 81-101.
3. Potoff, J. J., and Siepmann, J. I. (2001). Vapor–liquid equilibria of mixtures containing alkanes, carbon dioxide, and nitrogen. AICHE J. *47*, 1676-1682.
4. Mayo, S. L., Olafson, B. D., and Goddard, W. A. (1990). DREIDING: a generic force field for molecular simulations. J. Phys. Chem. *94*, 8897-8909.
5. Wilmer, C. E., Kim, K. C., and Snurr, R. Q. (2012). An Extended Charge Equilibration Method. J. Phys. Chem. Lett. *3*, 2506-2511.
6. Sarkisov, L., and Harrison, A. (2011). Computational structure characterisation tools in application to ordered and disordered porous materials. Mol. Simulat. *37*, 1248-1257.
7. Kikkinides, E. S., Kainourgiakis, M. E., Stefanopoulos, K. L., Mitropoulos, A. C., Stubos, A. K., and Kanellopoulos, N. K. (2000). Combination of small angle scattering and three-dimensional stochastic reconstruction for the study of adsorption–desorption processes in Vycor porous glass. J. Chem. Phys. *112*, 9881-9887.
8. Debye, P., and Bueche, A. M. (1949). Scattering by an Inhomogeneous Solid. J. Appl. Phys. *20*, 518-525.
9. Debye, P., Anderson Jr., H. R., and Brumberger, H. (1957). Scattering by an Inhomogeneous Solid. II. The Correlation Function and Its Application. J. Appl. Phys. *28*, 679-683.
10. Levitz, P., Ehret, G., Sinha, S. K., and Drake, J. M. (1991). Porous vycor glass: The microstructure as probed by electron microscopy, direct energy transfer, small-angle scattering, and molecular adsorption. J. Chem. Phys. *95*, 6151-6161.
11. Yeong, C. L. Y., and Torquato, S. (1998). Reconstructing random media. Phys. Rev. E *57*, 495-506.
12. Yeong, C. L. Y., and Torquato, S. (1998). Reconstructing random media. II. Three-dimensional media from two-dimensional cuts. Phys. Rev. E *58*, 224-233.
13. Jiao, Y., Stillinger, F. H., and Torquato, S. (2007). Modeling heterogeneous materials via two-point correlation functions: Basic principles. Phys. Rev. E *76*, 031110.
14. Jiao, Y., Stillinger, F. H., and Torquato, S. (2008). Modeling heterogeneous materials via two-point correlation functions. II. Algorithmic details and applications. Phys. Rev. E *77*, 031135.
15. Metropolis, N., Rosenbluth, A. W., Rosenbluth, M. N., Teller, A. H., and Teller, E. (1953). Equation of state calculations by fast computing machines. J. Chem. Phys. *21*, 1087-1092.
16. Friedli, S., and Velenik, Y. (2017). Statistical Mechanics of Lattice Systems: A Concrete Mathematical Introduction (Cambridge University Press).
17. Kierlik, E., Rosinberg, M., Tarjus, G., and Pitard, E. (1998). Mean-spherical approximation for a lattice model of a fluid in a disordered matrix. Mol. Phys. *95*, 341-351.
18. Woo, H.-J., and Monson, P. (2003). Phase behavior and dynamics of fluids in mesoporous glasses. Phys. Rev. E *67*, 041207.
19. Detcheverry, F., Kierlik, E., Rosinberg, M., and Tarjus, G. (2005). Helium condensation in aerogel: Avalanches and disorder-induced phase transition. Phys. Rev. E *72*, 051506.
20. Handford, T. P., Pérez-Reche, F. J., and Taraskin, S. N. (2013). Capillary condensation in one-dimensional irregular confinement. Phys. Rev. E *88*, 012139.
21. Handford, T. P., Dear, A., Pérez-Reche, F. J., and Taraskin, S. N. (2014). Effect of disorder on condensation in the lattice gas model on a random graph. Phys. Rev. E *90*, 012144.
22. Newman, M. E. J., and Barkema, G. T. (1999). Monte Carlo Methods in Statistical Physics (Clarendon Press).

23. Bortz, A. B., Kalos, M. H., and Lebowitz, J. L. (1975). A new algorithm for Monte Carlo simulation of Ising spin systems. J. Comput. Phys. *17*, 10-18.

24. Zhou, T., Ioannidou, K., Ulm, F.-J., Bazant, M. Z., and Pellenq, R. J.-M. (2019). Multiscale poromechanics of wet cement paste. Proc. Natl. Acad. Sci. USA *116*, 10652-10657.

25. Moghadam, P. Z., Rogge, S. M. J., Li, A., Chow, C.-M., Wieme, J., Moharrami, N., Aragones-Anglada, M., Conduit, G., Gomez-Gualdron, D. A., Van Speybroeck, V., and Fairen-Jimenez, D. (2019). Structure-Mechanical Stability Relations of Metal-Organic Frameworks via Machine Learning. Matter *1*, 219-234.

26. Chapman, K., Lapidus, S., and Chupas, P. (2015). Applications of principal component analysis to pair distribution function data. J. Appl. Crystallogr. *48*, 1619-1626.

27. Long, C. J., Bunker, D., Li, X., Karen, V. L., and Takeuchi, I. (2009). Rapid identification of structural phases in combinatorial thin-film libraries using x-ray diffraction and non-negative matrix factorization. Rev. Sci. Instrum. *80*, 103902.

28. O'Nolan, D., Huang, G., Kamm, G. E., Grenier, A., Liu, C.-H., Todd, P. K., Wustrow, A., Thinh Tran, G., Montiel, D., and Neilson, J. R. (2020). A thermal-gradient approach to variable-temperature measurements resolved in space. J. Appl. Crystallogr. *53*, 662-670.

29. Pedregosa, F., Varoquaux, G., Gramfort, A., Michel, V., Thirion, B., Grisel, O., Blondel, M., Prettenhofer, P., Weiss, R., Dubourg, V., Vanderplas, J., Passos, A., Cournapeau, D., Brucher, M., Perrot, and M., Duchesnay, É. (2011). Scikit-learn: Machine Learning in Python. J. Mach. Learn. Res. *12*, 2825-2830.

30. Hart, A., Hansen, T., and Kuhs, W. (2019). A hidden Markov model for describing turbostratic disorder applied to carbon blacks and graphene. Acta Crystallogr. A *75*, 501-516.

31. Lopes dos Santos, J. M. B., Peres, N. M. R., and Castro Neto, A. H. (2012). Continuum model of the twisted graphene bilayer. Phys. Rev. B *86*, 155449.

32. Willmott, P., Meister, D., Leake, S., Lange, M., Bergamaschi, A., Böge, M., Calvi, M., Cancellieri, C., Casati, N., and Cervellino, A. (2013). The materials science beamline upgrade at the swiss light source. J. Synchrotron Radiat. *20*, 667-682.

33. Ilavsky, J., and Jemian, P. R. (2009). Irena: tool suite for modeling and analysis of small-angle scattering. J. Appl. Crystallogr. *42*, 347-353.

34. Beaucage, G. (1996). Small-angle scattering from polymeric mass fractals of arbitrary mass-fractal dimension. J. Appl. Crystallogr. *29*, 134-146.

35. Myers, A. L., and Prausnitz, J. M. (1965). Thermodynamics of mixed-gas adsorption. AICHE J *11*, 121-127.

36. Osterrieth, J. W. M., *et al.* (2022). How reproducible are surface areas calculated from the BET Equation? Adv. Mater., 2201502.

37. Ma, Q., Zeng, L., Liu, X. Y., Zhuang, Q. X., and Qian, J. (2022). A simple and efficient method for preparing covalent organic framework aerogels with ultra-light and super-elastic. Microporous and Mesoporous Mater. *331*, 111623.

38. Zhu, D., Zhu, Y., Yan, Q., Barnes, M., Liu, F., Yu, P., Tseng, C.-P., Tjahjono, N., Huang, P.-C., Rahman, M. M., Egap, E., Ajayan, P. M., and Verduzco, R. (2021). Pure Crystalline Covalent Organic Framework Aerogels. Chem. Mater. *33*, 4216-4224.

39. Martín-Illán, J. Á., Rodríguez-San-Miguel, D., Castillo, O., Beobide, G., Perez-Carvajal, J., Imaz, I., Maspoch, D., and Zamora, F. (2021). Macroscopic Ultralight Aerogel Monoliths of Imine-based Covalent Organic Frameworks. Angew. Chem. Int. Ed. *60*, 13969-13977.

40. Wang, S., Zhang, C., Zhang, Z. Y., Yang, Y. H., Li, Q. L., Wang, W. J., Li, B. G., and Liu, P. W. (2021). Asymmetrical Exchange of Monomers for Constructing Hollow Nanoparticles and Antifragile Monoliths. Matter *4*, 618-634.

41. Li, C. X., Yang, J., Pachfule, P., Li, S., Ye, M. Y., Schmidt, J., and Thomas, A. (2020). Ultralight covalent organic framework/graphene aerogels with hierarchical porosity. Nat. Commun. *11*, 4712.

42. Mohammed, A. K., Usgaonkar, S., Kanheerampockil, F., Karak, S., Halder, A., Tharkar, M., Addicoat, M., Ajithkumar, T. G., and Banerjee, R. (2020). Connecting Microscopic Structures, Mesoscale Assemblies, and Macroscopic Architectures in 3D-Printed Hierarchical Porous Covalent Organic Framework Foams. J. Am. Chem. Soc. *142*, 8252-8261.

43. Zhao, W., Wang, T. P., Wu, J. L., Pan, R. P., Liu, X. Y., and Liu, X. K. (2019). Monolithic Covalent Organic Framework Aerogels through Framework Crystallization Induced Self-assembly: Heading towards Framework Materials Synthesis over All Length Scales. Chin. J. Polym. Sci. *37*, 1045-1052.

44. Ding, L. G., Yao, B. J., Li, F., Shi, S. C., Huang, N., Yin, H. B., Guan, Q., and Dong, Y. B. (2019). Ionic liquid-decorated COF and its covalent composite aerogel for selective CO_2 adsorption and catalytic conversion. J. Mater. Chem. A *7*, 4689-4698.

45. Liu, Z. S., Wang, H. W., Ou, J. J., Chen, L. F., and Ye, M. L. (2018). Construction of hierarchically porous monoliths from covalent organic frameworks (COFs) and their application for bisphenol A removal. J. Hazard. Mater. *355*, 145-153.

46. Liu, X. M., Lim, G. J. H., Wang, Y. X., Zhang, L., Mullangi, D., Wu, Y., Zhao, D., Ding, J., Cheetham, A. K., and Wang, J. (2021). Binder-free 3D printing of covalent organic framework (COF) monoliths for CO_2 adsorption. Chem. Eng. J. *403*, 126333.

47. Connolly, B. M., Aragones-Anglada, M., Gandara-Loe, J., Danaf, N. A., Lamb, D. C., Mehta, J. P., Vulpe, D., Wuttke, S., Silvestre-Albero, J., Moghadam, P. Z., Wheatley, A. E. H., and Fairen-Jimenez, D. (2019). Tuning porosity in macroscopic monolithic metal-organic frameworks for exceptional natural gas storage. Nat. Commun. *10,* 2345.

48. Finsy, V., Ma, L., Alaerts, L., De Vos, D., Baron, G., and Denayer, J. (2009). Separation of CO_2/CH_4 mixtures with the MIL-53 (Al) metal–organic framework. Microporous and Mesoporous Mater. *120*, 221-227.